The Sihailongwan maar Lake, northeastern China as a candidate Global Boundary Stratotype Section and Point for the Anthropocene Series

Journal:	*The Anthropocene Review*
Manuscript ID	ANR-22-0036.R1
Manuscript Type:	Global Boundary Stratotype Section and Point for the Anthropocene Series
Keywords:	Anthropocene, Artificial radioisotopes, GSSP, Sihailongwan Maar Lake, Varve Lamination
Abstract:	Sihailongwan maar Lake, located in Northeast China, is a candidate Global boundary Stratotype Section and Point (GSSP) for demarcation of the Anthropocene. The lake's varved sediments are formed by switching allogenic atmospheric inputs and authigenic lake processes and imprint environmental and human impacts at a continental-global scale. Varve counting and radiometric dating provided a precise annual-resolution sediment chronology for the site. Time series records of radioactive (^{239,240}Pu, ^{129}I, and soot ^{14}C), chemical (spheroidal carbonaceous particles, polycyclic aromatic hydrocarbons, soot, heavy metals, δ^{13}C, etc), physical (magnetic susceptibility and grayscale), and biological (environmental DNA) indicators all show rapid changes in the mid-20th century, coincident with lithological changes of the sediments from yellow to black. Statistical analyses of these proxies show a tipping-point in 1954 CE. ^{239,240}Pu activities follow a typical unimodal globally-distributed profile, and are proposed as the primary marker for the Anthropocene. A rapid increase in ^{239,240}Pu activities at 88 mm depth in core SHLW21-Fr-13 (1953±3 CE) is synchronous with rapid changes of other anthropogenic proxies and the Great Acceleration, marking the onset of the Anthropocene. The results indicate that Sihailongwan maar Lake is an ideal site for the Anthropocene GSSP.

The Sihailongwan maar Lake, northeastern China as a candidate Global Boundary Stratotype Section and Point for the Anthropocene Series

Abstract:

Sihailongwan maar Lake, located in Northeast China, is a candidate Global boundary Stratotype Section and Point (GSSP) for demarcation of the Anthropocene. The lake's varved sediments are formed by switching allogenic atmospheric inputs and authigenic lake processes and imprint environmental and human impacts at a continental-global scale. Varve counting and radiometric dating provided a precise annual-resolution sediment chronology for the site. Time series records of radioactive (^{239,240}Pu,^{129}I, and soot ^{14}C), chemical (spheroidal carbonaceous particles, polycyclic aromatic hydrocarbons, soot, heavy metals, δ^{13}C, etc), physical (magnetic susceptibility and grayscale), and biological (environmental DNA) indicators all show rapid changes in the mid-20th century, coincident with lithological changes of the sediments from yellow to black. Statistical analyses of these proxies show a tipping-point in 1954 CE. ^{239,240}Pu activities follow a typical unimodal globally-distributed profile, and are proposed as the primary marker for the Anthropocene. A rapid increase in ^{239,240}Pu activities at 88 mm depth in core SHLW21-Fr-13 (1953±3 CE) is synchronous with rapid changes of other anthropogenic proxies and the Great Acceleration, marking the onset of the Anthropocene. The results indicate that Sihailongwan maar Lake is an ideal site for the Anthropocene GSSP.

A plain word summary:

Sihailongwan maar Lake in NE China is an ideal site for the Global boundary Stratotype Section and Point (GSSP) of the Anthropocene. ^{239,240}Pu is recommended as the primary marker for the Anthropocene. Its rapid increase starting at a depth of 88 mm in core SHLW21-Fr-13 corresponds to the age of 1953±3 CE that marks the Holocene/Anthropocene boundary. This boundary is consistent with rapid changes observed in a wide range of other anthropogenic proxies.

Keywords:

Anthropocene, Artificial radioisotopes, GSSP, Sihailongwan maar Lake, Varve Lamination

Introduction

Sihailongwan maar Lake (SHLWML; Figures 1A-C) is a candidate succession proposed by the Anthropocene Working Group (AWG) for the Global boundary Stratotype Section and Point (GSSP) of the Anthropocene (Waters et al., 2018). The preparatory activities of the AWG, including events leading to the submission of GSSP proposals and the binding decision that the base of the Anthropocene should align with stratigraphic signals dating to the mid-20th century, are detailed in the introductory article of this special issue (Waters et al., 2022). SHLWML is a typical maar formed when groundwater and precipitation fill a volcanic crater. There are no fluvial inlets or outlets to SHLWML and minimal human disturbance due to the steep terrain of the crater walls. The lake sediments are varved (annually layered) and show distinct colour bands caused by deposition differences in winter and summer (Chu et al., 2005b; Chu et al., 2005a). Light-coloured detrital materials, or litho-siliciclastic, deposited on the ice/snow covered surface, enter the lake in spring when the surface ice melts, and dark-coloured organic materials characterize summer and fall sedimentation. Each varved interval with a packet of light siliciclastic, dark organics and algae constitutes an annual lamination (Chu et al., 2005b). These can be used to establish a chrono-stratigraphy and assess annual-scale climatic and environmental variations. Allogenic materials in the lake are dominantly from atmospheric deposition, and these alternate with authigenic organics. Chemical, physical and biological changes at a continental-global scale reflect natural and anthropogenic impacts that are preserved in these sediments.

Extensive studies have been conducted in SHLWML, and other maar lakes in the same volcanic province, to study climate change at millennial and centennial timescales (Mingram et al., 2018; Zhang et al., 2019a). Results suggest that the behaviour of proxies, including pollen and total organic carbon (TOC) in the modern period are different from what is observed in the Holocene. Distinct mid-20th century changes have been observed in nearby Xiaolongwan maar lake, including $\delta^{13}C$, planktonic to benthic (P:B) ratios, heavy metals and spheroidal carbonaceous particles (SCPs) (Panizzo et al., 2013), indicating widespread changes in composition and relative abundances of the materials deposited in multiple lakes. The natural geographical and environmental advantages of SHLWML make it suitable as a strategic site for the Anthropocene GSSP.

Here, we systematically investigate variations of multiple proxies including artificial radionuclides ($^{239,240}Pu$,^{129}I, soot ^{14}C); chemical features (SCPs, black carbon, char, soot, polycyclic aromatic hydrocarbon or PAHs, heavy metals, $\delta^{13}C$, $\delta^{15}N$, TOC, total nitrogen or TN, and C/N ratios), physical features (magnetic susceptibility or MS, and grayscale), and biological indicators (environmental DNA or eDNA) in sediment freeze cores collected from SHLWML. These results, together with a precise annual-scale chronology, provide a framework for the primary marker selection and highlight the advantages of the maar lake as the Anthropocene GSSP site.

Materials and methods

Geographic setting of core sites

SHLWML (E: 126°35'51"-126°36'24", N: 42°17'0"-42°17'24") is a low-rimmed volcanic crater lake (or maar lake) in Jingyu County, Jilin Province of NE China (Figures 1 and S1). It

is (1) a near-circular lake with a diameter of ~750 m, (2) relatively deep for its size (Figure 1C; maximum depth of ~50 m), and (3) located 797 m above sea level in the Long Gang Volcanic Field. The surrounding volcanic field covers 1700 km^2, and is a result of the Pacific Plate thrust beneath the Eurasian Plate. This collision resulted in 164 volcanic centers in the area (crater lakes, maars, and cones). The most recent eruption was at the Jinlongdingzi volcano, 15 km south of SHLWML, in 460 CE (Liu et al., 2009). SHLWML is one of a series of crater lakes in the volcanic field characterized by Quaternary alkali basalts (Figure 1B).

The climate in this region is driven by the East Asian monsoon (An et al., 2015). During the summer monsoon, moisture from the Pacific Ocean and Indian Ocean reaches this area; and in winter, its climate is controlled by the Siberian High (Figure S2). The mean annual temperature at the site is ~2-4 °C, and the average annual precipitation during 1971-2020 CE measured in the Jingyu County Meteorological station, about 20 km away from the SHLWM, is ~767 mm, concentrated in summer, from June to September (Figure 1D).

Today the area supports a dense conifer and broadleaf forest, and has been designated a national forest park since 1991 CE. The lake belongs to the Jilin Longwan National Natural Reserve with an area of 8102 hectares. There are heavy industries in Jilin Province, but the study area is minimally influenced by human activities. Jingyu County has a population of ~100,000 people, and is located ~20 km northeast of the lake. A paved road connects Jingyu County with SHLWML.

Field collection of core, sampling and core imagery

Coring of SHLWML was conducted in February, 2021 CE on the ice-covered lake surface. In total, 24 freeze cores, 50 to 80 cm in length, were collected in parallel using a freeze corer (Freezecorer for soft sediments, UWITEC GmbH, Austria) within an area of ~1,000 m^2 (E: 126°36′4.49″, N: 42°17′12.77″). Another four gravity cores, ~60 to 80 cm in length, were collected using a gravity corer (Core 60, UWITEC, Austria). Clear varves and sediment-water interfaces were observed in all cores (Figure S3), indicating minimal disturbance of the sediments. The cores were immediately stored in a mobile freezer (-36°C) and transported to the Institute of Earth Environment, Chinese Academy of Sciences (IEECAS) in Xi'an, China until analyses. The proposed GSSP (in core SHLW21-Fr-13) is archived in the IEECAS Core Repository room.

Chronological controls

For this study, we processed sediments from the top 20 cm, which cover the past ~210 years. There are two distinct marker layers occurring at depths of 5.5-6.0 and 7.0-8.0 cm in all cores (Figure S3). These light colourd bands are most likely composed of detrital material. These marker layers facilitate accurate intercomparison of chronological timeframes between the cores (Figure S3).

The core ages studied here are determined by varve dating. Sediments in the uppermost parts of the cores had high water contents, which made them fragile and unsuitable for direct varve counting. Thus, thin sections were made as follows: (1) the freeze core was cut into a frozen strip (20 × 2 × 2 cm) along the longitudinal direction and put in an aluminium box; (2)

it was freeze-dried, resin impregnated and hardened; (3) the hardened core strip was polished to a smooth surface and was cut into flakes (7 × 2 × 0.2 cm) along the longitudinal direction using a precision cutting machine (MECATOME T210, PRESI, France), with a 1-3 cm overlap between adjacent flakes for varve intercomparison (Chu et al., 2005a); (4) the flakes were adhered to glass slides, and then made into thin sections using a grinding and polishing machine (MECATECHECH 300, PRESI, France) until light could penetrate them to enable varve counting.

A trinocular stereo microscope with a camera system (Nikon, MSZ 1270, 8.6-80 X) was used to observe and take images of thin sections. These were oriented in the image and a depth scale was established. A dark organic layer along with a light detrital layer represents one year. Varves in the image were divided into three categories based on the varve quality index (VQI) (Bonk et al., 2015), VQI A: low quality, boundaries interrupted, counting difficult; VQI B: high quality, regular varves, boundaries slightly interrupted; VQI C: perfect quality, regular varves, boundaries parallel. Our varves are mainly composed of the last two types. Counts were made independently by three skilled individuals. For VQI B and C varves, they were directly added into the chronology with no uncertainty being added. For VQI A varves, 1 year uncertainty was added. Whether a varve could be included into the chronology was determined by a comparison of the counting results of the three individuals. Only when a varve was indicated by at least 2 persons it was added to the chronology (Żarczyński et al., 2018; Li et al., 2017). The final uncertainties were propagated from surface to bottom (Li et al., 2017).

Sub-samples were also taken at 2 mm intervals along the varve direction in the freeze cores in the IEECAS Core Repository room. Core dating (Figures 2A-F; SHLW21-Fr-13) included varve counting with high-resolution analyses of ^{210}Pb, ^{137}Cs and ^{226}Ra (most at 2 mm intervals with occasionally at 4 mm intervals) for cross validation on varve counting results (see SI for details).

Anthropocene proxies

A series of proxies (radioactive, physical, chemical, and biological) were measured as indicators of human influences at the Sihailongwan site. Radioactive proxies included plutonium (^{239,240}Pu), and iodine isotopes (^{129}I, ^{129}I/^{127}I), as well as soot ^{14}C. Physical proxies included grayscale and MS. Chemical analyses included micro-XRF scanning, novel materials such as spheroidal carbonaceous particles (SCPs), polycyclic aromatic hydrocarbons (PAHs), and black carbon (BC, and subtypes char and soot); organic matter including TOC, total nitrogen (TN), and the stable isotopes δ^{13}C and δ^{15}N; heavy metals including Pb, Cu, Zn, Cd, Hg, and Hg isotopes. Biological proxies included eDNA. The methodologies for these proxy analyses are summarized in Table 1 and a detailed description of the methods is presented in the supplementary information (SI). The core used for proxy measurements and the sample resolution are given in Table S1, while eDNA taxa are summarized in Table S2. In this study, almost all proxies were measured from freeze core samples at 2-4 mm intervals, except PAHs analyses conducted on a gravity core at 2.5 mm resolution (Table S1).

Numerical analysis

In order to investigate the relationships among the various proxies, correlations and classifications with different temporal variation patterns, Pearson correlation and Ward.D2

methods were applied ('vegan' package in R 3.5.1; available at https://www.r-project.org). Principal component analysis (PCA) included a Hellinger transformation method to reduce nonuniformity between the datasets. Principal components (PCs) and latent factors were calculated to understand the inter-relationships between proxies through time (Han et al., 2006). Time periods were categorized by their temporal variations expressed by the PCA. The main principal component (PC1) that explained most of the observed variance was plotted against time to visualize these temporal changes. In addition, the Pettitt test ("trend" package in R 3.5.1) was employed as a non-parametric test method (Rybski and Neumann, 2011), and an effective tool for analyzing trends and tipping-points through time (Bao et al., 2018).

Results

Lithology

SHLWML sediments are composed of detrital materials, organic matter and algae (Chu et al., 2005a). Distinct colour changes from the bottom to the top of the cores were observed in all cores (Figures 2E and S3). Colours gradually changed from yellow in the lower parts of the cores to dark-yellow bands and then darker colours in the upper sections. The dark-yellow layers began at a depth of 85 mm (core SHLW21-Fr-13, 1955–6 CE). The cause of the dark bands in the upper parts of the cores is likely related to decreasing dissolved oxygen concentrations over time, which commonly occurs in both the ocean and global lakes (Jane et al., 2021) due to thermal stratification in deep waters such as the SHLWML (50 m depth) under warmer water temperature. Reducing conditions in recent times would result in dark colour of lake sediments.

Grayscale measurements also show a decreasing trend toward the surface (Figure S4), in good agreement with the increase in dark layers in the upper parts of the cores. A continuously increasing MS trend upward is observed from a depth of ~89 mm in core SHLW21-FR-9 (ca. 1950 CE, Figure S4) and corresponds to an increase in heavy metals Pb and Zn (see below). A light colored marker layer mentioned above shows high grayscale and MS values at ~58-54 mm depth (1977-82 CE), consistent with the fact that these sediments are mainly siliciclastic, and allogenic magnetic mineral dominates the lake sediments (Thompson and Oldfield, 1986).

Core scanning results (Figures 3B-G) show no distinct changes for most elements in the mid-20th century. Only sulfur presents an increasing trend above a depth of 83 mm for core SHLW21-Fr-6 (equivalent to 1950 CE), but subsequently decreases above 23 mm (after 2004 CE). Most lithogenic elements (Fe, Si, K, Ca, Al, and Ti) have peak concentrations at 53 mm depth (1977–78 CE), corresponding to the siliciclastic marker layer, and then they decrease. This trend is in agreement with an overall decrease in dry bulk density (DBD; see SI for the measurements) (Figure 2D) as low DBD indicates less mineral matter.

Chronology

Varve counting of core SHLW21-Fr-13 produced a robust chronology (Figure 2E). The depth of 89 mm corresponds to 1950 CE with an uncertainty of ± 3 years. The lowest core depth (200 mm) we investigated in this study corresponds to 1808 CE, with an uncertainty of ± 6 year. This implies an average sedimentation rate (SR) of ~1 mm yr^{-1}, and the sub-sampling at 2 mm intervals for proxy analyses represents ~2 years on average

Excess ^{210}Pb (^{210}Pbex) activities, which are the measured total ^{210}Pb activity (^{210}Pbtotal) minus the supported ^{210}Pb activity (in equilibrium with ^{226}Ra), decreased exponentially with

depth (Figure 2B). There are two specific chrono-marker depths for ^{137}Cs (Figure 2C): (a) the onset of ^{137}Cs fallout at 88 mm depth (1953 CE), and (b) global nuclear weapons testing fallout peak at 77 mm depth (1964 CE). The two events were used as independent ages for calibrating the ^{210}Pb ages. A piecewise-constant rate ^{210}Pb supply model (CRS-pw) (Han et al., 2022; Tylmann et al., 2014) was used for radioactive chronological reconstructions. The two independent ^{137}Cs ages matched the varve counting ages (at 77 and 88 mm). We observed a dip in both ^{210}Pb and ^{137}Cs at ~57–62 mm, where the siliciclastic marker layer is located. This depth occurred at CRS-pw radioactive ages of ~1977–1983 CE, consistent with the varve counting dates.

A comparison of radionuclide dating and varve counting results for core SHLW21-Fr-13 shows comparable results for the post-1940 CE period (depth of 97 mm). However, at lower depths (below 97 mm), the radiometric dating tended to have relatively older ages compared with the varve counting results (Figure 2C). Considering the accuracy in annual time resolution and independence of the varve counting results, the varve-counting method is chosen for our chronology, and this also facilitates the comparison of ages among different cores as all the cores reported in this study have varve counting chronologies. The varve counting results show that uncertainties for upper part of the core SHLW21-Fr-13 (above 90 mm, corresponding to 1950 CE) range from 0-3 years, while for the lower part (90-200 mm, corresponding to 1810-1950 CE) the uncertainties are 3-6 years (see SI for uncertainty analyses of varve counting results).

Flux rates

The thickness of the top layer of core SHLW21-Fr-13 is equivalent to a sedimentation rate (SR) of 5 mm yr^{-1}, but the SRs decreased quickly with depth, reaching ~ 1 mm yr^{-1} at ~20 mm (Figure 2D). Relatively constant SRs (~ 1 mm yr^{-1}) are found for the lower parts of the core. The siliciclastic marker layer at ~61 mm corresponds to relatively low SR values.

DBD for core SHLW21-Fr-13 (Figure 2D) show an overall decreasing trend from the bottom to the top of the core, which is likely related to compaction and higher water content in the upper sediments of the lake. The highest DBD values are found in the siliciclastic layer (61 mm) due to large detrital material inputs, and relatively low SR values. The mass accumulation rates (MARs; Figure 2D) show relatively small variations in the lower parts of the cores. The highest MARs occurred at a depth of 57-62 mm (1977–83 CE), corresponding to the siliciclastic marker layer.

Radioisotopes

Plutonium. ^{239,240}Pu (^{239}Pu:$T_{1/2}$=24,100 yr, ^{240}Pu:$T_{1/2}$=6561 yr) profile in core SHLW21-Fr-13 (Figure 4A) showed a unimodal pattern, reflecting the global fallout of atmospheric nuclear weapons testing (ANWT). Constant and low ^{239,240}Pu activities were found for the lower part of the core (below 99 mm, 1940 CE). A rapid increase in ^{239,240}Pu activities was observed at and above 88 mm depth (since 1953 ± 3 CE), in agreement with a previous report on ^{239,240}Pu released by atmospheric nuclear weapons testing since 1952 CE (UNSCEAR, 2000). A large ^{239,240}Pu peak was observed at 79 mm, which corresponds to 1963 CE. Afterwards, ^{239,240}Pu activities decreased rapidly and then reached a consistently low level above ~67 mm depth (corresponding to 1970 CE). Measured ^{240}Pu/^{239}Pu atomic ratios in most

samples (>90%, excepting low-level values associated with ^{240}Pu analytical uncertainties) (Figure 4B) were in the range of global fallout (0.180 ± 0.014).

Iodine. ^{129}I concentrations in SHLWML sediments were very low (1.3×10^8 atoms/g) below 88 mm depth for core SHLW21-Fr-7 (before 1950 CE, Figure 4C). The low values represent naturally-produced ^{129}I in the pre-nuclear era. Above the depth of 88 mm (1950 ± 3 CE), ^{129}I activities and ^{129}I/^{127}I ratios significantly increased by two orders of magnitude compared to the pre-nuclear level. From 78-44 mm depth (1960s to early 1990s), ^{129}I showed large fluctuations superimposed on a persistent ^{129}I/^{127}I increase. From 44 mm depth upward (early 1990s to present), ^{129}I decreased and then rapidly increased, along with ^{127}I (R^2=0.88, $p<0.05$). Meanwhile, ^{129}I/^{127}I ratios decreased slowly and uniformly during this period, possibly due to a decrease in airborne ^{129}I released in the mid-1990s (Zhang et al., 2018) as nuclear fuel reprocessing plants in the former Soviet were decommissioned (Seversk from 1956–1995 CE and Zheleznogorsk from 1964–1995 CE) (Reithmeier et al., 2010).

Soot ^{14}C. Soot is an air pollutant that originates from the burning of fossil fuels and biomass and influences climate though its effects on the earth's radiative budget. Measured soot F^{14}C (fraction modern) values and calculated fossil fuel (FF) soot fractions (SI and (Han et al., 2022)) showed opposite patterns (Figure 4D). That is, high soot F^{14}C values were found to correspond to low FF soot factions and vice versa. The FF soot fraction increased from 10 to 25% in the 120–86 mm depth range in core SHLW21-Fr-13 (1910 to 1950 CE). After the People's Republic of China (PRC) was established at the end of 1949 CE, FF soot fractions rapidly increased and reached a peak of ~60% at 72 mm depth (~1964 CE). The FF soot fraction then decreased, from the start of the Great Cultural Revolution (GCR) in 1966 CE and during the subsequent economic recession (Wen, 2012). The lowest values are observed at 52 mm depth (1978 CE). The FF soot fraction increased following reforms that began in the late 1970s, with the opening of China, and peaked at 33 mm depth (2000 CE). The FF soot fractions then decreased, likely related to the desulfurization of factories in China that began in 2004 CE (Han et al., 2022; Zhang et al., 2019b).

Novel materials

Many novel materials are produced by human activities, often related to industrial production. Given a suitable chronostratigraphic framework, the study of these materials can be used to understand anthropogenic impacts through time.

SCPs are a component of fly-ash produced exclusively by coal and oil burning. SCP concentration profiles (Figure 5A) show a zero value below 93 mm depth in the SHLW21-Fr-1 core (before ~1940 CE) and a rapid increase in concentration and flux (not shown) above a depth of 86 mm (1950 CE). The highest concentrations and fluxes were found in SHLWML sediments at 42 mm depth (early 1990s). During the past three decades, theconcentrations and fluxes of SCPs have decreased continuously. The U-shaped SCPs profile versus depth is similar to what was found for the FF soot faction.

PAHs are mainly produced during fossil fuel and biomass burning, but they also have natural sources (Han et al., 2015). We measured 29 different PAH species in the lake sediments. The sum of 16 parent (unsubstituted) PAHs, low-molecular-weight (LMW-; 2–3 rings) and high-molecular-weight (HMW-; 4–7 rings) PAHs (see SI for details). These all showed

constant and low concentrations below 86 mm depth (before 1950 CE) in the SHLW20-6 gravity core (Figures 5B–D). These compounds started to increase with the industrial period that accompanied the establishment of the PRC, and reached a plateau in the depth interval from 67-55 mm (during the GCR: late 1960s to late 1970s). After that period, they continued to increase and peaked at 38 mm depth (end of the 20th century), and then decreased due to the implementation of pollution controls in 2005 CE and further restrictions in 2012 CE. The overall PAH profiles with depth are very similar to those of FF soot fractions and SCPs, with U-shape trends. In fact, with the exception of perylene, all of the parent-PAHs showed a similar pattern.

BC originates only from the burning of fossil fuels and biomass (see SI). It is composed of two subtypes, char and soot (Han et al., 2007). Char particles are combustion residues that are mainly biomass burning emissions and are representative of local conditions, while soot particles are combustion condensates from both fossil fuel and biomass burning emissions. Soot particles are typically smaller than char and more readily transported over long distances than char (Han et al., 2010). Constant and low soot concentrations were observed below 86 mm depth (before 1950 CE) in core SHLW21-Fr-1 and showed a pattern similar to the PAHs. An overall increasing soot trend was found above 86 mm depth (after 1950 CE), while char decreased (Figure S5). The highest soot concentration was observed at 35 mm depth (1997 CE), followed by an overall decrease.

Organic matter proxies

Neither the TOC and TN concentrations nor the C/N ratios showed clear patterns in the sediment profiles (Figures 6A-E), but large fluctuations for these substances were observed in the top 20 mm of core SHLW21-Fr-2. This may be caused by high sedimentation rates at the top of the core (one year representing 5 mm deposition relative to sampling intervals of 2 mm), which could result in the separation of clastic layers from organic and algal layers in different samples. Variations with depth were observed for the stable organic carbon isotopes (Figure 6D), which showed an overall decrease above a depth of 85 mm in core SHLW21-Fr-2 (after 1950 CE). The most negative $\delta^{13}C$ values were seen at 37 mm depth (1996-7 CE). $\delta^{15}N$ showed a decrease above 77 mm depth (after 1960 CE), with an increasingly rapid change above a depth of 49 mm (1980 CE; Figure 6E). The lowest value occurred at 28 mm depth (~2004 CE), followed by fluctuations in recent decades.

Inorganic geochemical signals

Heavy metal concentrations of Pb, Cu, Zn, and Cd showed increasing trends starting at a depth of 90 mm (1950 CE) in core SHLW21-Fr-9 (Figures 7A-D). Further increases in these elements occurred above a depth of 53 mm (after 1982 CE). The highest heavy metal concentrations were found in sediments deposited at 36 mm depth (early 2000s).

Hg concentrations and accumulation rates (not shown) increased significantly above a depth of ~160 mm (1860s) in the SHLW21-Fr-2 core (Figure 7E). The mean accumulation rate above a depth of 85 mm (establishment of the PRC in late 1949 CE) was 21.8 ± 5.1μg m^{-2} yr^{-1}, which is approximately 2.2 to 3.0 times higher than the values from 1860–1949 CE (9.8 ±

1.5 μg m^{-2} yr^{-1}) and the pre-industrial period (7.2 ± 0.9 μg m^{-2} yr^{-1}), respectively, which is in agreement with previous studies in North America and Europe (Lindeberg et al., 2007; Lepak et al., 2020). Similar to other heavy metals, there were distinct minima in Hg concentrations at ~57 mm (late 1970s) associated with low industrial activities during the end of GCR period. These also correspond to the siliciclastic marker layer, followed by rapid increases associated with rapid economic development.

Changes in Δ^{200}Hg values (the even-mass independent fractionation or MIF signature) in sediments was generally small (0.04 to 0.17‰, mean = 0.10 ± 0.03‰) throughout the core SHLW21-Fr-2 (Figure 7G). Δ^{199}Hg and Δ^{201}Hg values showed distinct positive shifts at ~160 mm (the 1860s; Figures 7F and 7H). Above 57 mm, that is, after the later 1970s, the Δ^{199}Hg and ^{201}Hg values showed marked decreases (Figures 7F and 7H).

Biotic markers

eDNA records in sediment core SHLW21-Fr-14 were investigated to explore changes in biomass, phytoplankton diversity, and community composition (Figures 8A-D). There was an overall decreasing trend in eDNA composition above 110 mm depth (since 1920s) and further reductions above 90 mm depth (after 1950 CE). The Shannon index of phytoplankton, which can indicate biological diversity (Wang et al., 2012), also decreased rapidly above 90 mm depth (1950 CE). This is similar to the change in PC1 (which explained 53.75% of the phytoplankton community structure change) calculated with PCA conducted on the whole phytoplankton species composition data. This indicates a structural change in the phytoplankton community composition around 1950 CE, confirmed by the tip-pointing analysis (Figures 8C and 8D).

Statistical results

Strong correlations were found among the heavy metals, PAHs, SCPs, soot, soot FF fractions, MS, ^{129}I, δ^{13}C, and eDNA (Figure 9A). These proxies can all be considered as indicators of anthropogenic perturbations. Other proxies including organic matter TOC, OC and δ^{15}N, ^{239,240}Pu, ^{137}Cs, mercury isotopes, and char showed weaker correlations with the above proxies. ^{239,240}Pu and ^{137}Cs are specific to atmospheric nuclear tests (now banned) and thus did not track with the other proxies after nuclear weapon testing ceased.

With regard to sample classification of different time periods, the PCA (Figure 9B) produced two components that separated the time periods into pre-1953 CE and post-1953 CE. A successive analysis of the first principal component (PC1) scores for the period 1880–2021 CE (Figures 9C and D) based on the Pettitt test, showed a significant tipping-point at 1954 CE.

Discussion

Chronology The varve counting results closely correspond to the ^{210}Pb and ^{137}Cs dating, thus providing an accurate annual-resolution chronology. Minor differences in varve counts for different cores were observed mostly within 0–4 mm depth, which may be due to the uncompacted nature of the surface sediments.

Extensive deforestation over the Longwan region in 1977 and 1978 CE coincides with the siliciclastic marker layer. At that time, many forests were cleared for agriculture, while later the region became reforested. Deforestation may have caused an increase in detrital material inputs, resulting in ^{210}Pb and ^{137}Cs concentrations decreases (Figure 2A). Similar patterns of low ^{210}Pb and ^{137}Cs activities have been reported for other lakes in the same region (Chu et al., 2005a; Panizzo et al., 2013; Schettler et al., 2006b). This suggests a regional distribution of the siliciclastic marker layer, providing an auxiliary chrono-stratigraphic control (Figure 2).

Radioisotopes ^{239,240}Pu profiles in SHLWML sediments follows a trend similar to other sites around the world (Waters et al., 2018; Wu et al., 2010; Zhuang et al., 2019; Liao et al., 2014), reflecting their global distribution, and the suitability as a global marker of the onset of the Anthropocene. The ^{239,240}Pu peak was 2 mm deeper than the ^{137}Cs peak (Figure 4A, 77 versus 79 mm, both measured in core SHLW21-Fr-13), equivalent to an offset of ~1–2 years. This is in contrast to results from Tsukuba, Japan that found both peaks in 1963 CE (Hirose et al., 2008). The difference between the two studies may be explained by differences in the behavior of the isotopes in aquatic environments, which leads to more rapid deposition of particle-bound Pu compared with water-soluble Cs. The distribution coefficient of ^{137}Cs (100–500 g cm^{-3}) is about two to three orders of magnitude lower than that for Pu (10^4–10^5 g cm^{-3}) (Krishnamurthy et al., 2001). The more particle-reactive Pu can be incorporated into sediments more rapidly than Cs, even though both reached the lake at the same time.

A residence time of about 1 year in lake water has been estimated for ^{137}Cs, with 150 days in the epilimnion and 280 days in the hypolimnion (Wieland et al., 1993). Hence, peak ^{137}Cs values in SHLWML sediments record the year 1964 CE, and this date is used here. On the other hand, the ^{239,240}Pu peak is more likely from 1963 CE, due to its particle affinity and direct deposition.

Anthropogenic ^{129}I (half-life of 15.7 Ma) can be identified from abrupt increases above pre-nuclear values. This anthropogenic ^{129}I was produced by nuclear weapons testing and subsequent additions primarily from releases associated with nuclear fuels reprocessing. The vertical ^{129}I profile in SHLWML sediments is similar to sediment cores taken in western Europe, and East and South Asia (Aldahan et al., 2007; Fan et al., 2016; Zhang et al., 2018). All of these results show significant increases in the 1950s, confirming global fallout sources from early nuclear weapons testing. ^{129}I and ^{129}I/^{127}I ratios increased by more than two orders of magnitude above pre-nuclear values in the core, and more recent sediments contain ^{129}I mainly from European nuclear fuel reprocessing plants through long-distance atmospheric deposition.

It has been proposed that iodine can migrate in sediments due to degradation of organic matter and changes in redox conditions (Aldahan et al., 2007), and that this might limit its application as a primary marker for the Anthropocene. However, our results do not show obvious vertical ^{129}I migration in SHLWML sediments. This may be related to the strong anoxic environment of SHLWML, which has high organic matter, clays, iron and aluminum oxides, favorable for iodine preservation (Chu et al., 2005b; Schettler et al., 2006a). Our results demonstrate that ^{129}I provides a good record of atmospheric deposition. Such records of anthropogenic ^{129}I have also been observed in corals, and tree rings, among other natural archives (Bautista et al., 2016; Bautista et al., 2018; Mitsuguchi et al., 2021; Reithmeier et al.,

2006; Zhao et al., 2019). Taken together, these records provide robust global and continental signals of human nuclear activities, from the mid-20th century to the present.

Both ^{239,240}Pu and ^{129}I in the environment are released from the nuclear weapons testing and have a clear global distribution, while ^{129}I also originates from the nuclear fuel reprocessing process, showing a continental distribution. Both ^{239,240}Pu and artificial ^{129}I can indicate the beginning of the Anthropocene, while ^{129}I can serve as a useful marker for human nuclear activities in the post-ANWT era.

Fossil fuel and biomass combustion products Proxies including SCPs, PAHs, and BC as well as the BC subcomponents char and soot are all combustion products, but some PAHs we studied also have natural sources. Among these combustion products, SCPs come solely from fossil fuel combustion, while PAHs and soot are mainly from fossil fuels in modern times, and char is mainly from biomass burning. Thus, SCPs, PAHs including HMW- and LMW-PAHs, and soot all have similar profiles in SHLWML, with a typical U-shape. Before 1950 CE, they are found at low and constant concentrations, and subsequently increased, with peak values in the late 1990s, and a subsequent decrease. The temporal trends in SHLWML SCPs match records from many other areas of the world (Rose, 2015), indicating emissions from industrial sources on a global scale. However, we should note that there are still some differences in their temporal variations for the combustion products. For example, there was a peak in soot concentration in ~2010 CE, while SCPs and PAHs concentrations decreased at that time. This may be related their different emission factors under similar combustion conditions and they may have different transport processes in the intermediary.

Although the history of soot and PAH distributions on a global scale is still unknown, we anticipate that they follow a similar pattern, with increases associated with industrialization and decreases associated with pollution controls. Early data suggest this is true for soot. In European countries, peak soot emissions happened during the 1960s and then decreased rapidly (Bond et al., 2007; Novakov and Hansen, 2004). In China, the highest soot concentrations in SHLWML sediments happened around 2000 CE and then decreased. This pattern is seen in the FF soot fraction in both SHLWML (Figure 4D) and Huguangyan maar Lake (southern China, over 2,000 km distant) (Han et al., 2022),. Both show an increasing FF soot fraction trend followed by more recent decreases in this century (Figure S6). The highest soot concentrations in SHLWML sediments occurred at 39 mm depth (1997 CE).

Unlike the constant and low soot concentrations during the pre-1950 period, the FF soot fraction increased during that period, reaching as high as ~25% of FF contributions. This may be due to transport from Europe. Before World War II, industrialization was focused in developed countries where FF soot was produced, then transported eastward by westly winds. Similar to other novel materials, the highest FF soot fractions were observed during 1997-2003 CE, and then decreased due to pollution controls. FF soot fractions decreased more slowly than SCPs. In this region, FF soot is derived from both coal burning and motor vehicle emissions, while SCPs originate mainly from coal burning. In recent decades, coal emissions in China have decreased, but vehicular emissions have increased (Han et al., 2016).

Char differs from soot as it comes mainly from biomass burning and follows an overall decreasing trend since the mid-20th century, reflecting a decrease in biomass burning in NE China over the past 70 years. This trend is consistent with the overall increase in FF contributions of soot mentioned above, also evident in soot/char ratios (Figure S5D), with high

ratios indicating a greater FF contribution (Han et al., 2010). Diagnostic ratios of individual PAHs can indicate energy sources. For example, HMW-/LMW-PAHs ratios (Figure 5E) show an increasing trend that accelerated after 1950 CE, from increasing fossil fuel usage associated with industrialization in China; while after the 1990s, fossil fuel consumption dropped and these ratios decreased, also seen in the FF soot fractions (Figure 4D).

Heavy metals Industrial emissions have been the dominant source for most heavy metals although Pb came mainly from leaded fuel used by automobiles (Xu et al., 2012). As expected, Pb, Cu, Zn, Cd and Hg showed similar variations in SHLWML, with a sharp overall increasing trend that began ~1950 CE, followed by decreases in recent decades, similar to the U-shaped pattern of the novel materials. Hg concentrations are exceptional, as they show a significant increase since the 1860s (Figure 7E). Elemental mercury exists almost exclusively as a gas, and can be transported over long-distances. Thus, historical Hg concentration trends potentially reflect temporal changes over continental or global scales. Δ^{199}Hg and Δ^{201}Hg values show positive shifts in the 1860s, which reflect increasing primary and secondary anthropogenic emissions associated with early industrialization (Streets et al., 2017). Δ^{199}Hg values above 62 mm (after the late 1970s) show a notable decrease (Figure 7F), possibly related to Hg isotopic fractionation during aqueous Hg transformation. Changes in industrial activities related to the opening-up of China in the late 1970s may also have affected the isotopic composition of Hg emissions.

All of the heavy metals show large dips in concentration at ca. 1980 CE, which may be due to two factors: 1) the economic crisis after the GCR, and 2) the appearance of the light-coloured siliciclastic marker layer (~1977-78 CE), composed of clastic materials. These two factors combined to produce the lowest heavy metal concentrations in the profile, also observed for other proxies, including SCPs, PAHs, soot, TOC, and TN. In general, heavy metal profiles show temporal trends associated with changes in the types and magnitudes of industrial emissions both in China and around the globe.

Organic proxies and biomarkers Sediment organic matter and biomarkers are generally indirect indicators of human impacts (Waters et al., 2018). TOC, TN and their ratios show no clear temporal pattern in SHLWML profiles (Figures 6A-C), indicating minimal change in surrounding biomass and authigenous organics. However, δ^{13}C and δ^{15}N follow overall depletion trends, at different times. The δ^{13}C depletion (~1950 CE) occurred before δ^{15}N depletion (~1960 CE to the late 1970s) (Figures 6D and E). These trends are in good agreement with previous reports of global δ^{13}C and δ^{15}N preserved in sediments, corals, tree rings and ice cores, among other archives (Swart et al., 2010; Loader et al., 2013; Rubino et al., 2013; Black et al., 2011; Wolfe et al., 2013; Hastings et al., 2009; Waters et al., 2018; Holtgrieve Gordon et al., 2011). These records tend to show earlier δ^{13}C and δ^{15}N changes than those we observed, but follow similar patterns. The consensus view of these proxies is that they are associated with anthropogenic inputs of radiocarbon-dead and ^{13}C-depleted CO_2 from fossil fuel combustion for δ^{13}C and the use of fossil fuels and fertilizers for δ^{15}N.

The lowest δ^{13}C values observed at our site coincided with the highest soot and PAHs concentrations and FF soot fractions (~1996-7 CE), suggesting that regional industrial emissions impacted the local biomass through atmospheric CO_2 exchange, and caused a δ^{13}C depletion in sediments. The lowest δ^{15}N occurred at ~2004 CE. After that time desulfurization

and denitration of coal-fired plants were implemented in China. Denitration likely caused a positive shift in $\delta^{15}N$ in the SHLWML sediments.

The continuous decrease in eDNA since around 1950 CE (Figure 8A) suggests that biological productivity has decreased in recent decades. Moreover, the observed eDNA profiles (Figure 8B) are very similar to the results reported for *Pinus* spp. and coniferous tree pollen in Lake Sanjiaolongwan sediments (Zhang et al., 2019a), which confirm that allogenous biomass inputs contribute to the eDNA composition. Apart from the decrease in biomass input indicated by palynological results (Zhang et al., 2019a), reduced biological production and low eDNA may also have been affected by stratification in deep lakes like SHLWML, exacerbated by global warming (Yan et al., 2020). Phytoplankton diversity significantly decreased after 1950 CE (Figure 8B), possibly from climate warming. The reversed profiles of the Shannon index (increasing trend), which was used to reflect phytoplankton diversity (see SI for explanation), and eDNA PC1 score (decreasing trend), which indicates temporal pattern change in phytoplankton community structure (see SI for explanation), after the late 1990s (Figure 8B) are similar with those ("U"-shaped) from fossil fuel products such as FF soot fractions, PAHs, and SCPs. This likely indicates the impact of rising fossil fuels on phytoplankton diversity and the biomass.

Our results suggest that while TOC, TN and TOC/TN ratios are not ideal markers for the Anthropocene, TOC and TN isotopes, and eDNA may serve as useful anthropogenic proxies.

Considerations of a GSSP at SHLWML

A summary graph of the key proxies from SHLWML sediments indicates that a variety of our GSSP proxies show rapid changes since the mid-20th century in SHLWML sediments (Figures 10A-G). As discussed above, these proxies could serve as Anthropocene markers, but to provide an optimal GSSP boundary for the Anthropocene, we need a definitive global marker. Plutonium isotopes ($^{239,240}Pu$) meet this requirement. These are complemented by radiogenic ^{129}I in SHLWML sediments, as they both exhibit similar trends at the onset of the Anthropocene around 1953 CE, and these are global in nature. ^{129}I can also be used to track large-scale anthropogenic inputs that continue to the present day. However, atmospheric-sourced $^{239,240}Pu$ may be expected to provide optimal time resolution for the boundary, as it is particle-bound, and rapidly enters the sediments. Once in the sediments Pu isotopes stay there as Pu is not readily soluble. Thus, we follow the recommendation by the Anthropocene Working Group (AWG) (Zalasiewicz et al., 2017) and select $^{239,240}Pu$ as the primary marker for the Anthropocene, while other anthropogenic proxies $^{129}I/^{127}I$ ratio, SCPs, PAHs, FF soot fraction, elemental Pb, and Shannon index of phytoplankton in eDNA provide us with valuable secondary markers (Figure 10).

The rapid increase in $^{239,240}Pu$ activities at 88 mm in core SHLW21-Fr-13 (GSSP candidate), correspond to 1953 ± 3 CE, and this point is suggested as the onset of the Anthropocene in this study. There are several reasons we chose this date. First, it is consistent with the statistical results conducted for all measured proxies (Figure 9C), which exhibited a tipping point in 1954 CE. This time is also very close to the visible lithological boundary in SHLWML cores, that show a clear black band or belt starting at 85-86 mm depth (1955–56 CE, Figure 10) near the onset of the Anthropocene. Furthermore, this timeframe encompasses the Great Acceleration in the mid-20th century and the dawn of the Nuclear Age, reflecting global environmental perturbations unseen in human history.

One crucially important implication of our results—and those from related studies—is that the developing countries may be among the strategic choices for the Anthropocene GSSP selection. Large-scale temporal changes in anthropogenic inputs are clearly evident at SHLWML as summarized above. The timing of the Great Acceleration overlaps with the initial industrialization in China and other developing countries, creating global environmental change. Thus, SHLWML sediments reflect environmental and climate change at continental or even larger scales and would be an ideal choice for the Anthropocene GSSP. The SHLWML site satisfies a broad range of GSSP requirements endorsed for the Quaternary (Head and Gibbard, 2015; Remane et al., 1996), and applicable to the Anthropocene. These include: (1) an optimal primary ^{239,240}Pu marker and numerous secondary markers, all consistent with the age ~1953 CE; (2) a sufficiently high sedimentation rate, 88 mm thickness (1953-2021 CE), to measure a wide variety of primary and auxiliary proxies with good time resolution; (3) continuous sedimentation through time proven by the chronological reconstruction; (4) annual varve laminations that provide an accurate chronology, internally consistent with radiometric ages; (5) a stable depositional environment; (6) abundance and diversity of well-preserved biotic (eDNA) materials; (7) an Anthropocene boundary marked by ^{239,240}Pu and a visible lithologic boundary that is consistent with all other isotopic, chemical, and biological proxies; (8) extensive studies for both the proposed GSSP and many lakes in the surrounding region; (9) a site located in a well-protected National Park Reserve, easily accessible by scientific researchers now and in the future, and further sampling could be easily done there.

Summary

1. SHLWML sediments are varved with annual laminations. Integrated varve counting, radioisotope dating, and distinct marker layers enabled the reconstruction of a reliable, annual-scale chronology for SHLWML cores. Thus, it facilitates detailed temporal comparisons of a wide variety of anthropogenic proxies.

2. SHLWML sediments receive allogenic materials almost exclusively through atmospheric deposition, and thus they reflect natural and anthropogenic influences at continental to global scales. Given that plutonium isotopes (^{239,240}Pu) preserve a global fallout signal, are rapidly deposited from the atmosphere, and are chemically inert, we selected them as the primary Anthropocene marker. Other anthropogenic proxies such as ^{129}I/^{127}I, SCPs, PAHs, FF soot fraction, elemental Pb, and phytoplankton Shannon index have profiles reflecting human impacts at regional, continental and global scales, and are recommended as secondary Anthropocene markers.

3. We propose to mark the onset of the Anthropocene by a distinct rapid increase in ^{239,240}Pu in core SHLW21-Fr-13 at 88 mm depth, in 1953 ± 3 CE. This time point is very close to the time when rapid changes in other anthropogenic proxies began, with a statistical tipping point in 1954 CE, corresponding to the Great Acceleration. A colouration change from yellow to black sediments occurs just above our proposed GSSP (1955-56 CE) in SHLWML, which locates 2 mm higher than the GSSP location defined by ^{239,240}Pu's fast increase, providing a useful visible boundary marker.

We propose the name, "Sihailongwan stage" for the Anthropocene stratotype section.

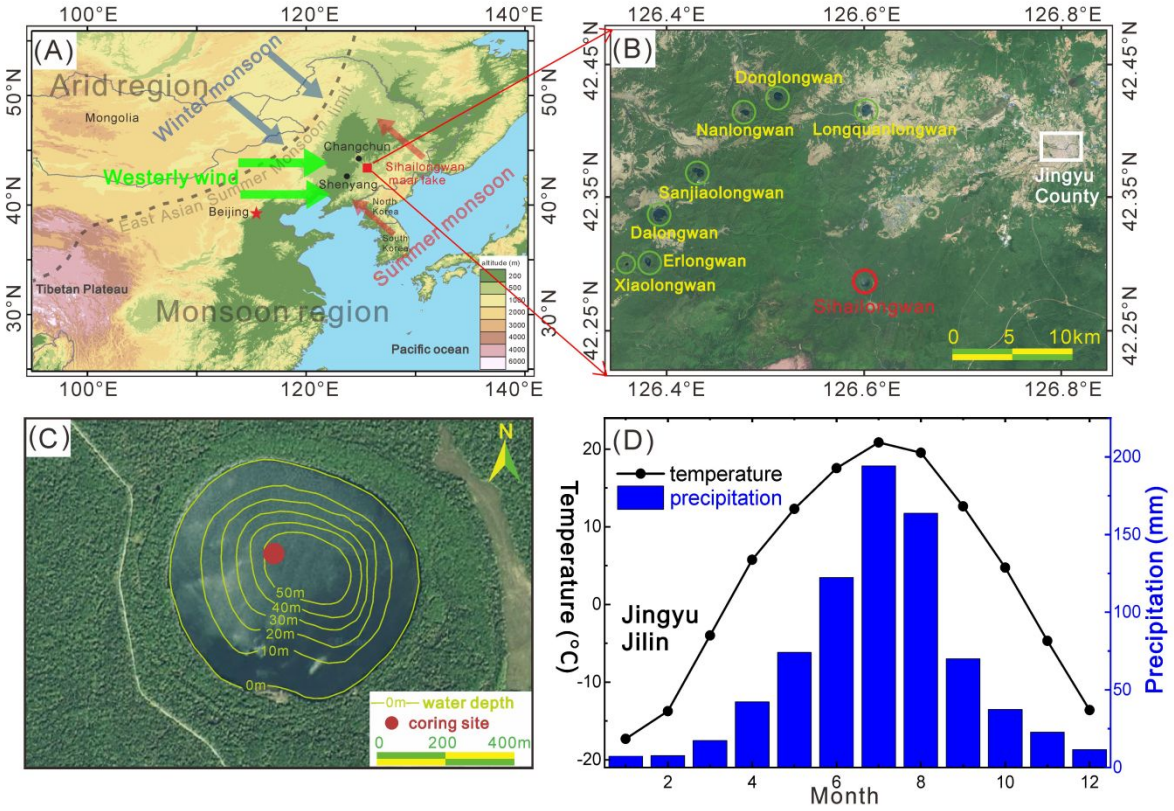

Figure 1. Location of Sihailongwan maar Lake in Jingyu County, Jilin Province of NE China. (A) the climate system of Sihailongwan maar Lake, mainly influenced by the east Asian monsoon and Westerlies; (B) a series of crater lakes in the Longwan Volcanic Field; (C) contour map of Sihailongwan maar Lake; the red dot shows the sampling location where 24 parallel sediment cores were taken; and (D) monthly precipitation and temperature variations during 1971–2020 CE in Jingyu County, about 20 km away from Sihailongwan maar Lake (data from the Jingyu County Meteorological station).

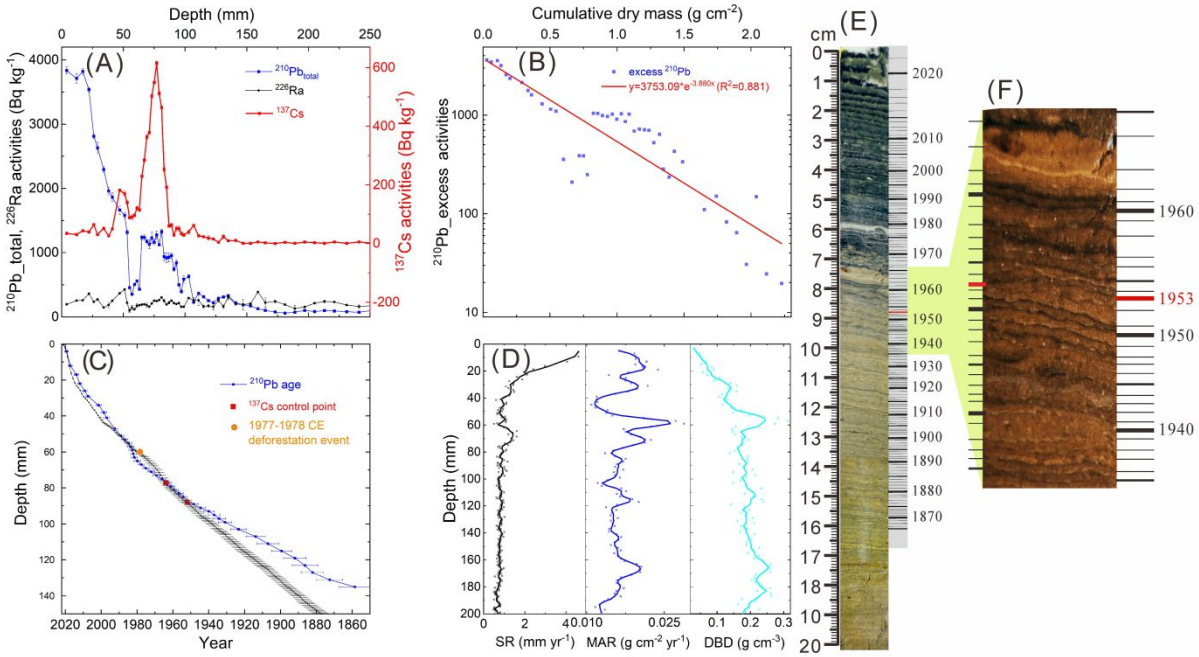

Figure 2. Chronological results for core SHLW21-Fr-13 from Sihailongwan maar Lake. (A) ^{210}Pb_total, ^{137}Cs, and ^{226}Ra activities; (B) exponential distribution of ^{210}Pb_excess activities (measured total ^{210}Pb activities minus ^{226}Ra activities); (C) comparison of chronology from varve counting (black line) and radioactive dating (coloured line) reconstructed using a piecewise-constant rate ^{210}Pb supply model (CRS-pw); (D) sedimentation rate (SR), mass accumulation rate (MAR) and dry bulk density (DBD) ; (E) varve counting results of depth versus age; and (F) enlarged picture of varves during 1935-1965 CE, with enhanced contrast ratio and brightness.

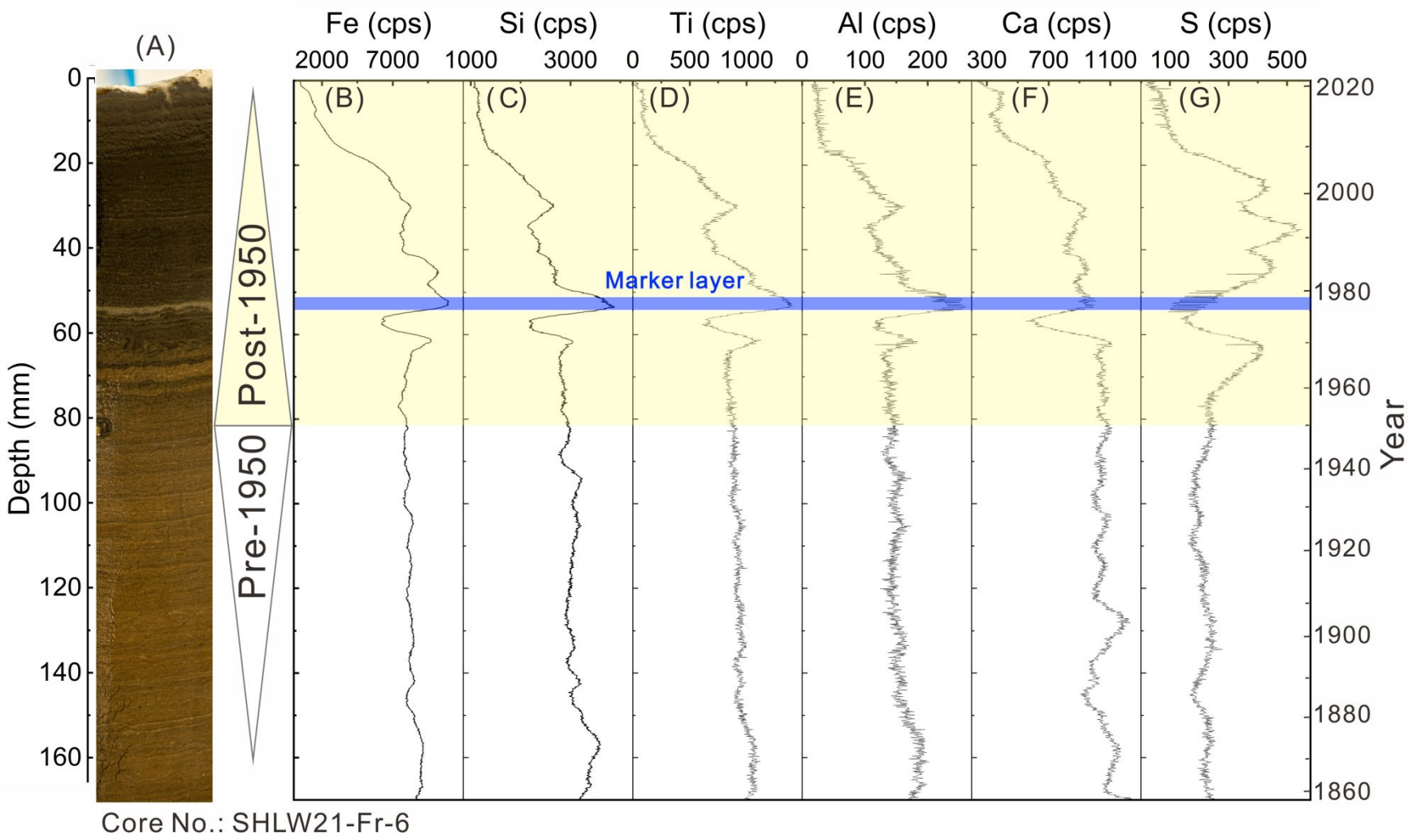

Figure 3. Lithological composition (A) and micro-XRF scan results of different elements (B-G) from sediment core SHLW21-Fr-6 in Sihailongwan maar Lake.

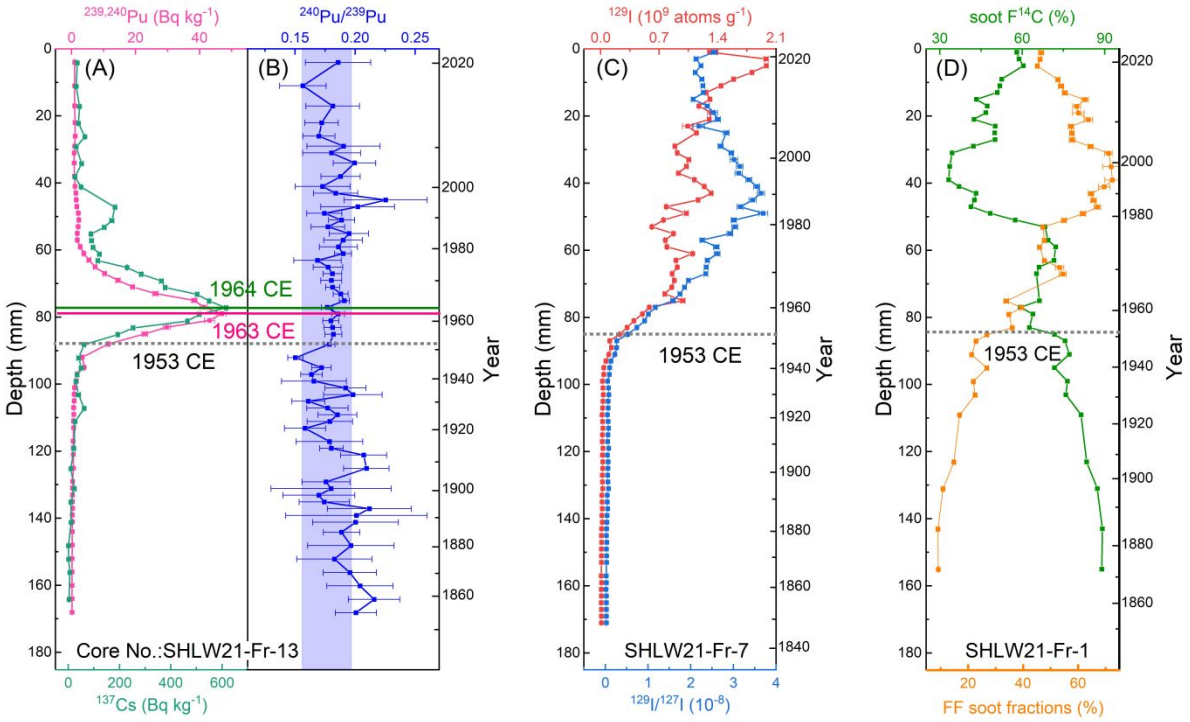

Figure 4. Variations of radionuclides activities versus depth and age in sediment cores from Sihailongwan maar Lake. (A) ^{239,240}Pu and ^{137}Cs activity concentrations; (B) ^{240}Pu/^{239}Pu ratios in core SHLW21-Fr-13; (C) ^{129}I and ^{129}I/^{127}I in core SHLW21-Fr-7; and (D) soot F^{14}C and calculated fossil fuel (FF) soot fractions in core SHLW21-Fr-1. Error bars of the proxies in the figures indicate uncertainties. The horizontal dashed line indicates year 1953 ± 3 CE, highlighting the rapid increase in ^{239,240}Pu and ^{129}I activities at that time. The vertical light blue area in panel B indicates the range of global fallout ^{240}Pu/^{239}Pu (0.180 ± 0.014).

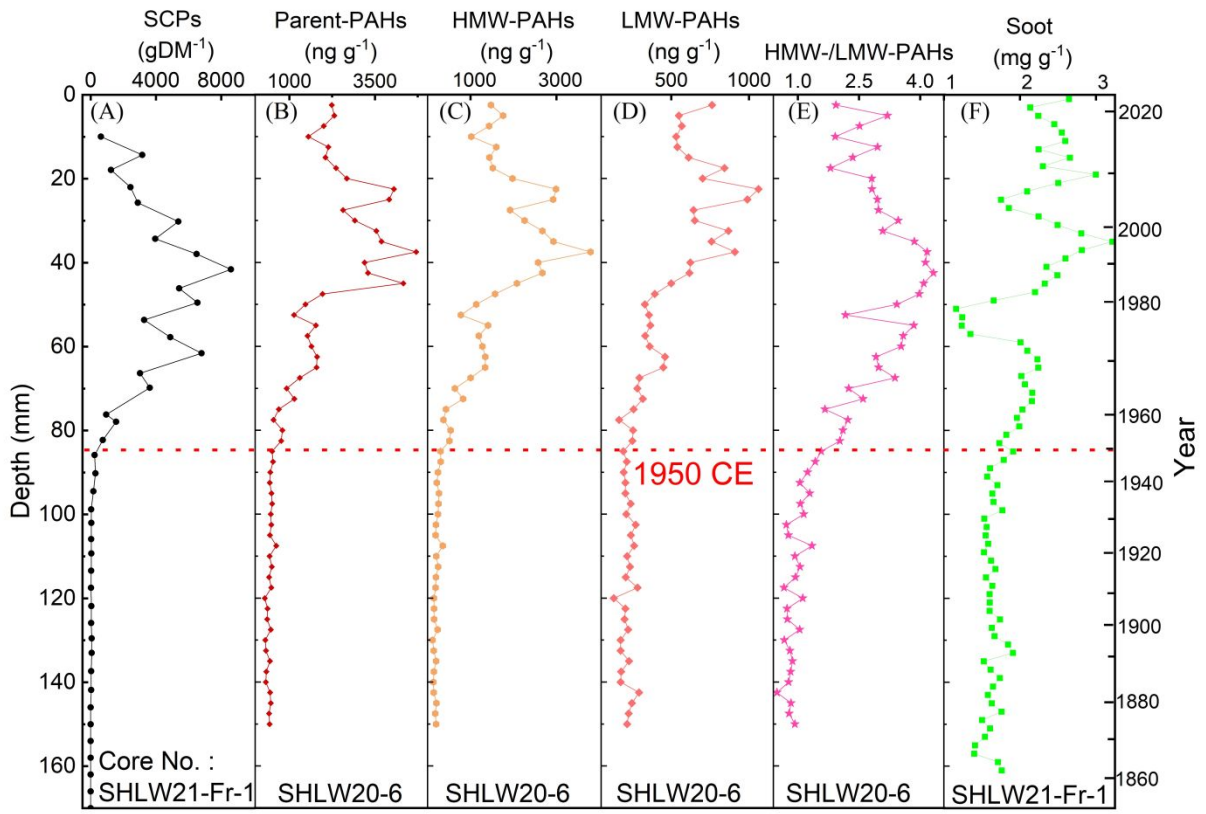

Figure 5. Variations of novel materials versus depth and age in sediment cores from Sihailongwan maar Lake. (A) concentrations of spheroidal carbonaceous particles (SCPs) in core SHLW21-Fr-1; (B-D) concentrations of parent polycyclic aromatic hydrocarbons (parent-PAHs), high- (4-7 ring) and low-molecular weight (HMW- and LMW-) PAHs; (E) ratio of HMW-/LMW-PAHs in core SHLW20-6, a gravity core with a chronology following the core SHLW21-Fr-1; (F-G) concentrations of soot and char; and (H) soot/char ratios in core SHLW21-Fr-1. The horizonal dotted line marks the fast increase in anthropogenic proxies since the mid-20th century (1950 CE).

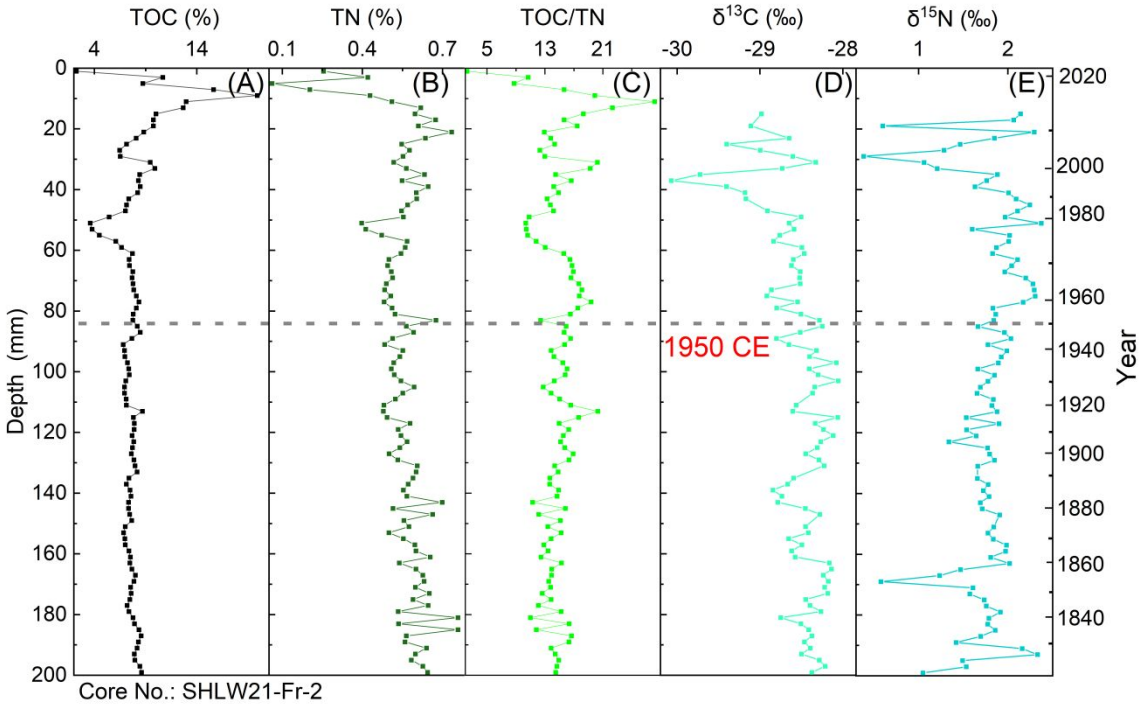

Figure 6. Depth distributions of total organic carbon (TOC), total nitrogen (TN) and their isotopic signatures ($\delta^{13}C$ and$\delta^{15}N$) in sediment core SHLW21-Fr-2 from Sihailongwan maar Lake. (A) total organic carbon (TOC) concentrations; (B) total nitrogen concentrations; (C) ratios of TOC/TN; (D-E) $\delta^{13}C$ and $\delta^{15}N$. The horizonal dotted line marks the fast increase in anthropogenic proxies since the mid-20th century (1950 CE).

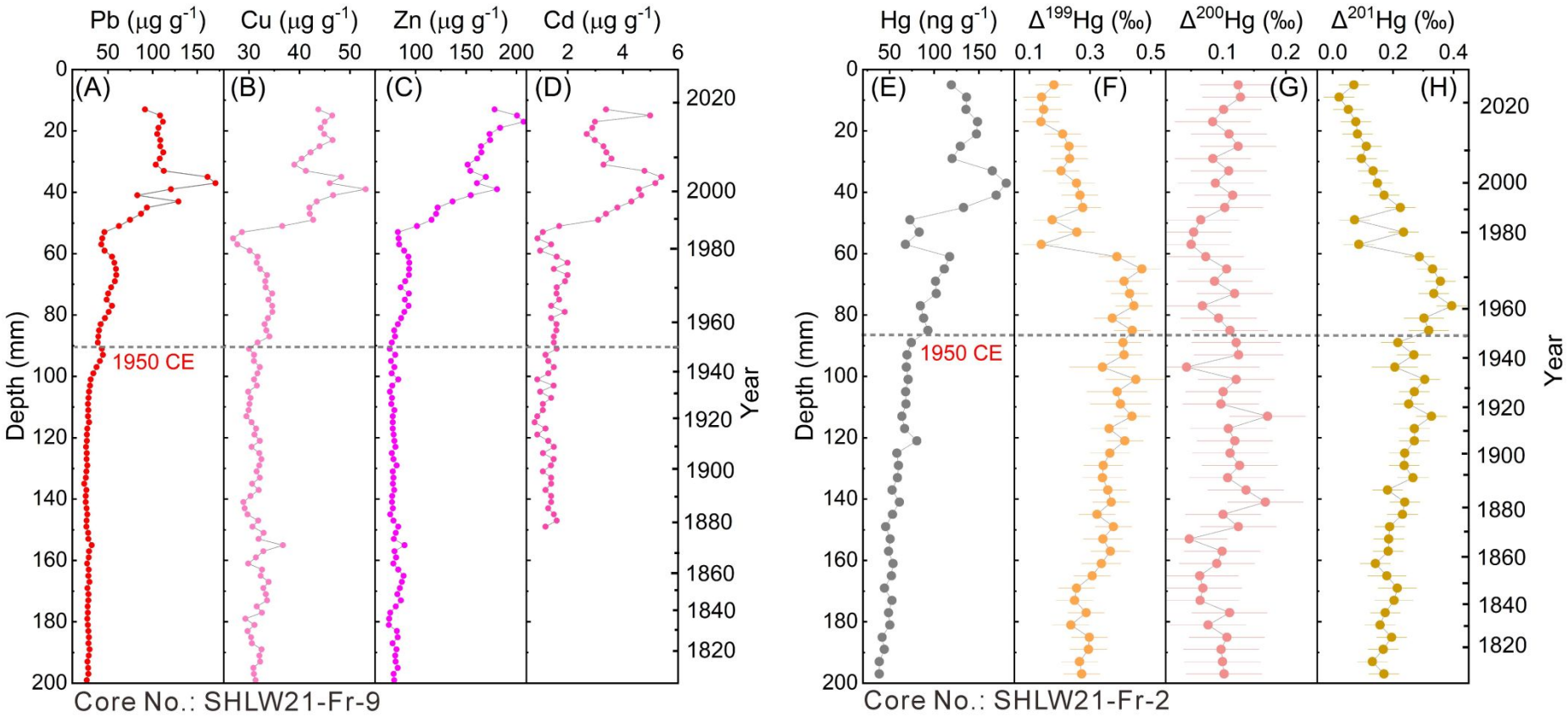

Figure 7. Depth distributions of heavy metals and mercury isotopes in sediment cores from Sihailongwan maar Lake. (A-D) Pb, Cu, Zn and Cd concentrations in core SHLW21-Fr-9; (E-I) Hg concentrations and Hg isotopic signatures in core SHLW21-Fr-2. The horizonal dotted line marks the fast increase in anthropogenic proxies since the mid-20th century (1950 CE).

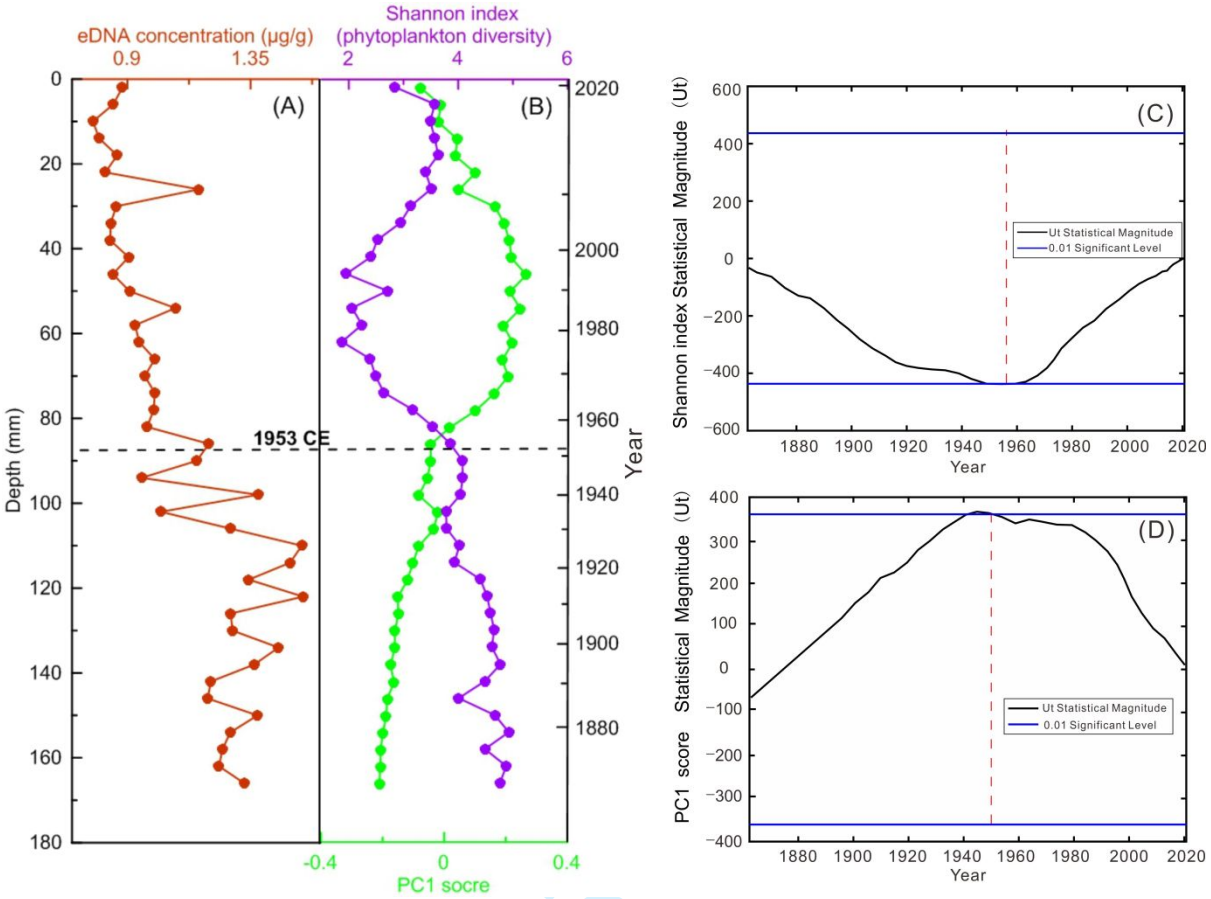

Figure 8. Vertical profiles of sedimentary DNA content and diversity and community structure changes in phytoplankton in core SHLW21-Fr-14 from Sihailongwan Lake. (A) environmental DNA concentrations; (B) Shannon index of the phytoplankton diversity (purple curve), and PC1 (green curve) extracted from the PCA (principal component analyses) based on the phytoplankton composition data; (C-D) Pettitt statistical temporal tipping point of the Shannon index and PC1 of phytoplankton composition, with vertical red lines indicating tipping point.

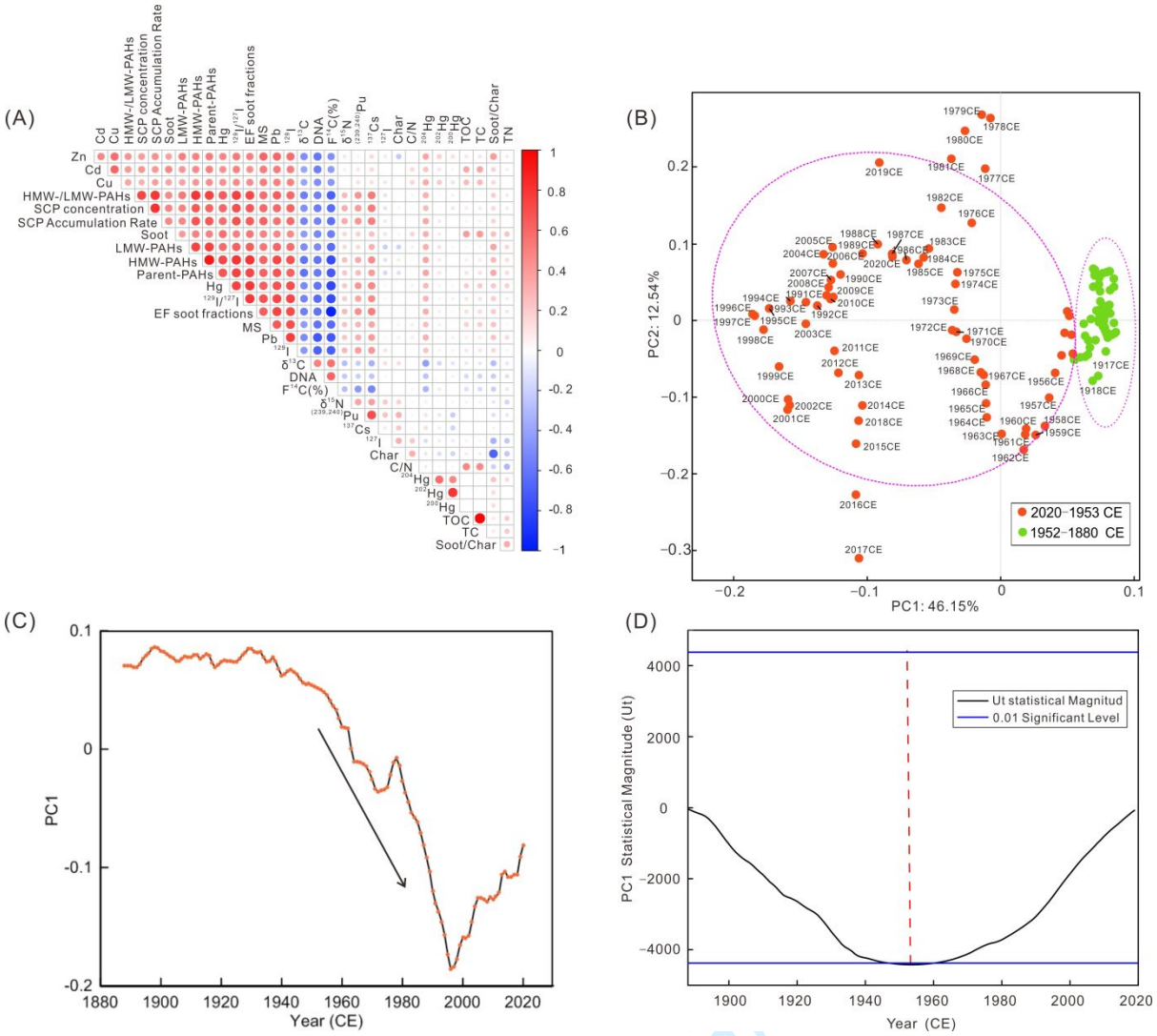

Figure 9. Statistical analyses of proxy categories and their temporal tipping point. (A) correlation and classification among different proxies based on Pearson correlation and Ward.D2 cluster methods; (B) classification of temporal variations based on the scores of PCA (principal component analysis) components PC1 (principal component 1, the dominant component) and PA2 (principal component 2); (C) temporal variations of PC1; and (D) Pettitt tipping point analyses of PC1 at a significance level of 0.01 showing tipping point at ~1954. The vertical dashed line corresponds to the timing of the tipping-point.

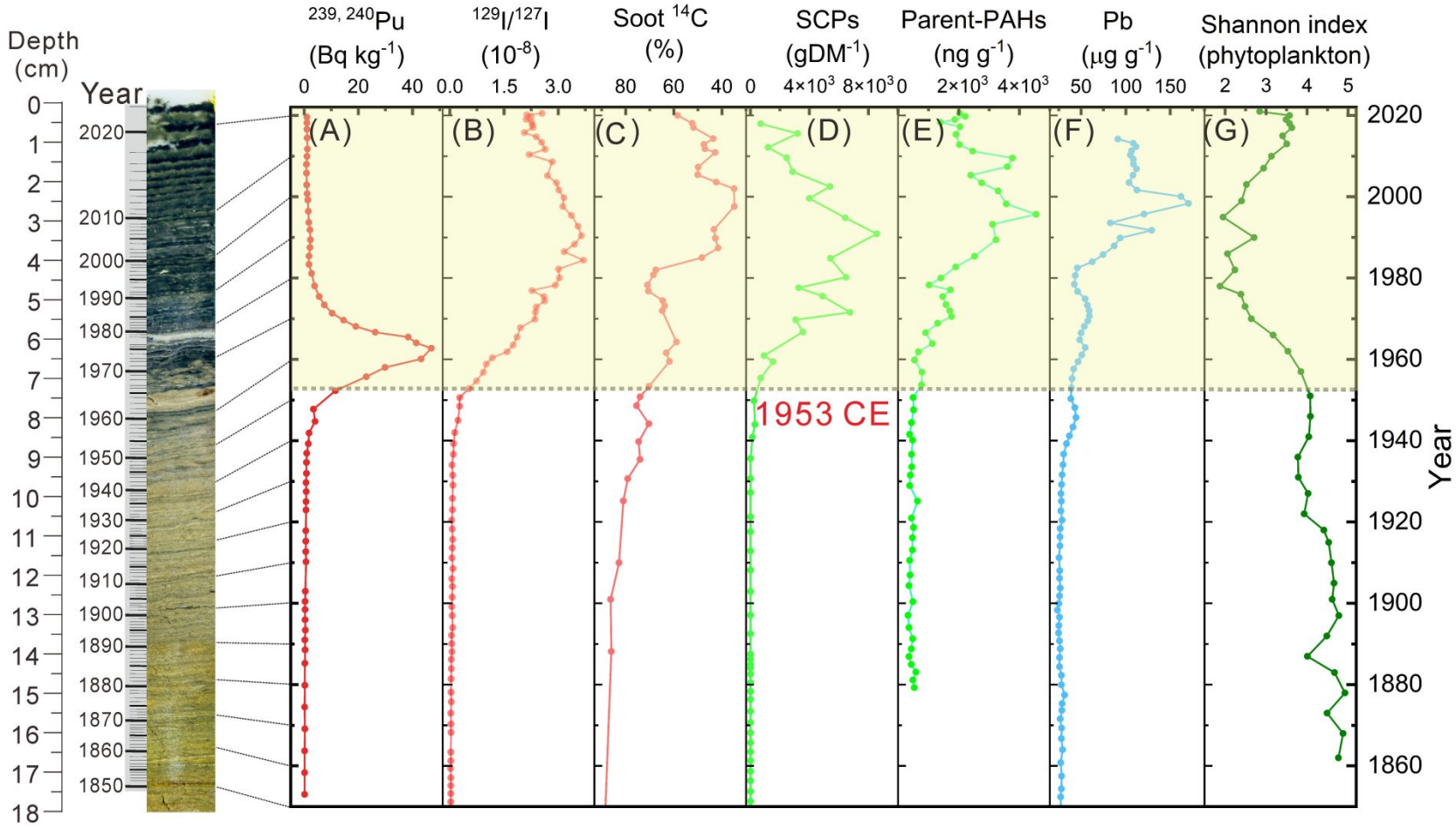

Figure 10. Variations in the lithology and proxies influenced by human activities after the mid-20th century as reconstructed from sediments from Sihailongwan maar Lake, Jilin Province of NE China. Left image shows varves of core SHLW21-Fr-13; (A) $^{129}I/^{127}I$; (B) $^{239,240}Pu$; (C) soot ^{14}C; (D-H) SCPs, parent-PAHs, heavy metal Pb, and Shannon index of phytoplankton in eDNA. $^{239,240}Pu$ was selected as the primary marker for the Anthropocene, marking the onset of the Anthropocene at a depth of 88 mm in core SHLW21-Fr-13, corresponding to 1953 ± 3 CE. Other proxies were selected as secondary Anthropocene makers.

Table 1. Anthropocene proxies used in this study and analytical methods with corresponding core numbers. SI = additional information given in supplementary material.

Item	Proxies	Methods	References	Core No.
Lithology	Magnetic susceptibility	Bartington MS2 meter	(Dearing et al., 1996)	SHLW21-Fr-9
	Grayscale	HD Photography	SI	SHLW21-Fr-13
Chronology	^{210}Pb, ^{137}Cs	Gamma spectrometry	(Appleby, 2001); (Tylmann et al., 2014)	SHLW21-Fr-13
	Varve dating	Thin section-varve counting	(Chu et al., 2005a)	SHLW21-Fr-1, 2, 7, 8, 9, 13, 14
Flux rates	Mass accumulation rates	Calculated by varve counting results and dry bulk density	SI	SHLW21-Fr-13
	Sedimentation rate	Varve counting	SI	SHLW21-Fr-13
Radioisotopes	Plutonium isotopes	ICP-MS	(Xing et al., 2018)	SHLW21-Fr-13
	Iodine isotopes	AMS (^{129}I), ICP-MS (^{127}I)	(Zhang et al., 2018)	SHLW21-Fr-7
	^{14}C in soot	AMS	(Han et al., 2022)	SHLW21-Fr-1
Novel materials	SCPs	Microscope Counting	(Rose, 2008)	SHLW21-Fr-1
	29-PAHs	GC-MS	(Han et al., 2015)	SHLW20-6
	Black carbon	IMPROVE	(Han et al., 2007)	SHLW21-Fr-1
Organic matter proxies	Total organic carbon, Total nitrogen,	Elementa DIN-19539	SI	SHLW21-Fr-2 SHLW21-Fr-2
	Stable carbon and nitrogen isotope	IRMS	(Liu et al., 2011);	SHLW21-Fr-2
Inorganic geochemical signals	Inorganic elements	XRF	SI	SHLW21-Fr-9
	Hg isotope	Nu Plasma MC-ICP-MS	(Fu et al., 2019)	SHLW21-Fr-2
	Elements	resin impregnation-XRF core scanning	(Richter et al., 2006)	SHLW21-Fr-6
Biotic markers	eDNA	Quibt 3.0, Miseq sequencing	(Yan et al., 2020)	SHLW21-Fr-14

Please refer to the supplementary information for the abbreviations in the Table.

References:

Aldahan A, Englund E, Possnert G, et al. (2007) Iodine-129 enrichment in sediment of the Baltic Sea. *Applied Geochemistry* 22(3): 637-647.

An Z, Wu G, Li J, et al. (2015) Global monsoon dynamics and climate change. *Annual Review of Earth and Planetary Sciences* 43: 29-77.

Appleby P (2001) Chronostratigraphic techniques in recent sediments. In: Last WM and Smol JP (eds) *Tracking environmental change using lake sediments*. Berlin, Heidelberg: Springer, pp.171-203.

Bao W, Shen D, Ni P, et al. (2018) Proposition and certification of moving mean difference method for detecting abrupt change points. *Acta Geographica Sinica* 73(11): 2075-2085.

Bautista AT, Matsuzaki H and Siringan FP (2016) Historical record of nuclear activities from I-129 in corals from the northern hemisphere (Philippines). *Journal of Environmental Radioactivity* 164: 174-181.

Bautista AT, Miyake Y, Matsuzaki H, et al. (2018) High-resolution 129I bomb peak profile in an ice core from SE-Dome site, Greenland. *Journal of Environmental Radioactivity* 184-185: 14-21.

Black D, Thunell R, Wejnert K, et al. (2011) Carbon isotope composition of Caribbean Sea surface waters: Response to the uptake of anthropogenic CO2. *Geophysical Research Letters* 38(16): L16609.

Bond TC, Bhardwaj E, Dong R, et al. (2007) Historical emissions of black and organic carbon aerosol from energy-related combustion, 1850-2000. *Global Biogeochemical Cycles* 21(2): GB2018.

Bonk A, Tylmann W, Goslar T, et al. (2015) Comparing varve counting and 14C-AMS chronologies in the sediments of Lake Żabińskie, northeastern Poland: Implications for accurate 14C dating of lake sediments. *Geochronometria* 42: 1733-8387.

Chu G, Gu Z, Xu B, et al. (2005a) Varve chronology and radiometric dating (137Cs, 210Pb) from the Sihailongwan Maar, Northeastern China (In Chinese with English Abstract). *Quaternary Sciences* 25: 202-207.

Chu GQ, Liu JQ, Schettler G, et al. (2005b) Sediment fluxes and varve formation in Sihailongwan, a maar lake from northeastern China. *Journal of Paleolimnology* 34(3): 311-324.

Dearing JA, Dann RJL, Hay K, et al. (1996) Frequency-dependent susceptibility measurements of environmental materials. *Geophysical Journal International* 124(1): 228-240.

Fan Y, Hou X, Zhou W, et al. (2016) I-129 record of nuclear activities in marine sediment core from Jiaozhou Bay in China. *Journal of Environmental Radioactivity* 154: 15-24.

Fu X, Zhang H, Liu C, et al. (2019) Significant seasonal variations in isotopic composition of atmospheric total gaseous mercury at forest sites in China caused by vegetation and mercury sources. *Environmental Science & Technology* 53(23): 13748-13756.

Han Y, An Z, Arimoto R, et al. (2022) Sediment soot radiocarbon indicates that recent pollution controls slowed fossil fuel emissions in southeastern China. *Environmental Science & Technology* 56: 1534-1543.

Han YM, Cao JJ, Chow JC, et al. (2007) Evaluation of the thermal/optical reflectance method for discrimination between char- and soot-EC. *Chemosphere* 69: 569-574.

Han YM, Cao JJ, Lee SC, et al. (2010) Different characteristics of char and soot in the atmosphere and their ratio as an indicator for source identification in Xi'an, China. *Atmospheric Chemistry and Physics* 10(2): 595-607.

Han YM, Chen LWA, Huang RJ, et al. (2016) Carbonaceous aerosols in megacity Xi'an, China: Implications of thermal/optical protocols comparison. *Atmospheric Environment* 132: 58-68.

Han YM, Du PX, Cao JJ, et al. (2006) Multivariate analysis of heavy metal contamination in urban dusts of Xi'an, Central China. *Science of the Total Environment* 355(1-3): 176-186.

Han YM, Wei C, Bandowe BAM, et al. (2015) Elemental carbon and polycyclic aromatic compounds in a 150-Year sediment core from Lake Qinghai, Tibetan Plateau, China: Influence of regional and local sources and transport pathways. *Environmental Science & Technology* 49(7): 4176-4183.

Hastings MG, Jarvis JC and Steig EJ (2009) Anthropogenic impacts on nitrogen isotopes of ice-core nitrate. *Science* 324(5932): 1288.

Head MJ and Gibbard PL (2015) Formal subdivision of the Quaternary System/Period: Past, present, and future. *Quaternary International* 383: 4-35.

Hirose K, Igarashi Y and Aoyama M (2008) Analysis of the 50-year records of the atmospheric deposition of long-lived radionuclides in Japan. *Applied Radiation and Isotopes* 66(11): 1675-1678.

Holtgrieve Gordon W, Schindler Daniel E, Hobbs William O, et al. (2011) A coherent signature of anthropogenic nitrogen deposition to remote watersheds of the northern hemisphere. *Science* 334(6062): 1545-1548.

Jane SF, Hansen GJA, Kraemer BM, et al. (2021) Widespread deoxygenation of temperate lakes. *Nature* 594(7861): 66-+.

Krishnamurthy RV, Machavaram M, Baskaran M, et al. (2001) Organic carbon flow in the Ob, Yenisey rivers and Kara Sea of the arctic region. *Marine Pollution Bulletin* 42(9): 726-732.

Lepak RF, Janssen SE, Engstrom DR, et al. (2020) Resolving atmospheric mercury loading and source Trends from isotopic records of remote North American lake sediments. *Environmental Science & Technology* 54(15): 9325-9333.

Li K, You H and Liu X (2017) Review on lake sediment varve chronology in China (in Chinese with English abstract). *Journal of Lake Science* 29: 266-275.

Liao H, Bu W, Zheng J, et al. (2014) Vertical distributions of radionuclides (Pu239+240, Pu-240/Pu-239, and Cs-137) in sediment cores of Lake Bosten in northwestern China. *Environmental Science & Technology* 48: 3840-3846.

Lindeberg C, Bindler R, Bigler C, et al. (2007) Mercury pollution trends in subarctic lakes in the northern Swedish mountains. *Ambio* 36(5): 401-405.

Liu J, Chu G, Han J, et al. (2009) Volcanic eruptions in the Longgang volcanic field, northeastern China, during the past 15,000 years. *Journal of Asian Earth Sciences* 34(5): 645-654.

Liu W, Wang Z, Wang Z, et al. (2011) Variations in nitrogen isotopic values among various particle-sized fractions in modern soil in northwestern China. *Chinese Journal of Geochemistry* 30(3): 295.

Loader NJ, Young GHF, Grudd H, et al. (2013) Stable carbon isotopes from Torneträsk, northern Sweden provide a millennial length reconstruction of summer sunshine and its relationship to Arctic circulation. *Quaternary Science Reviews* 62: 97-113.

Mingram J, Stebich M, Schettler G, et al. (2018) Millennial-scale East Asian monsoon variability of the last glacial deduced from annually laminated sediments from Lake Sihailongwan, NE China. *Quaternary Science Reviews* 201: 57-76.

Mitsuguchi T, Okabe N, Yokoyama Y, et al. (2021) $^{129}I/^{127}I$ and Δ14C records in a modern coral from Rowley Shoals off northwestern Australia reflect the 20th-century human nuclear activities and ocean/atmosphere circulations. *Journal of Environmental Radioactivity* 235-236: 106593.

Novakov T and Hansen JE (2004) Black carbon emissions in the United Kingdom during the past four decades: an empirical analysis. *Atmospheric Environment* 38(25): 4155-4163.

Panizzo VN, Mackay AW, Rose NL, et al. (2013) Recent palaeolimnological change recorded in Lake Xiaolongwan, northeast China: Climatic versus anthropogenic forcing. *Quaternary International* 290: 322-334.

Reithmeier H, Lazarev V, Ruehm W, et al. (2010) Anthropogenic I-129 in the atmosphere: Overview over major sources, transport processes and deposition pattern. *Science of the Total Environment* 408(21): 5052-5064.

Reithmeier H, Lazarev V, Rühm W, et al. (2006) Estimate of European 129I releases supported by 129I analysis in an Alpine ice core. *Environmental Science & Technology* 40(19): 5891-5896.

Remane J, Bassett MG, Cowie J, et al. (1996) Revised guidelines for the establishment of global chronostratigraphic standards by the International Commission on Stratigraphy (ICS). *Episodes* 19: 77-81.

Richter T, van der Gaast S, Koster B, et al. (2006) The Avaatech XRF core scanner: Technical description and applications to NE Atlantic sediments. *Geological Society London Special Publications* 267: 39-50.

Rose NL (2008) Quality control in the analysis of lake sediments for spheroidal carbonaceous particles. *Limnology and Oceanography-Methods* 6: 172-179.

Rose NL (2015) Spheroidal carbonaceous fly ash particles provide a globally synchronous stratigraphic marker for the Anthropocene. *Environmental Science & Technology* 49(7): 4155-4162.

Rubino M, Etheridge DM, Trudinger CM, et al. (2013) A revised 1000 year atmospheric δ13C-CO2 record from Law Dome and South Pole, Antarctica. *Journal of Geophysical Research: Atmospheres* 118(15): 8482-8499.

Rybski D and Neumann J (2011) A review on the Pettitt test Pettitt-test. In: Kropp J and Schellnhuber H-J (eds) *In extremis: Disruptive events and trends in climate and hydrology*. Berlin, Heidelberg: Springer Berlin Heidelberg, pp.202-213.

Schettler G, Liu Q, Mingram J, et al. (2006a) Palaeovariations in the east-asian monsoon regime geochemically recorded in varved sediments of Lake Sihailongwan (Northeast China, Jilin Province). Part 1: Hydrological conditions and dust flux. *Journal of Paleolimnology* 35(2): 239-270.

Schettler G, Mingram J, Negendank JFW, et al. (2006b) Palaeovariations in the East-Asian Monsoon regime geochemically recorded in varved sediments of Lake Sihailongwan (Northeast China, jilin Province). Part 2: a 200-year record of atmospheric lead-210 flux variations and its palaeoclimatic implications. *Journal of Paleolimnology* 35(2): 271-288.

Streets D, Horowitz H, Jacob D, et al. (2017) Total mercury released to the environment by human activities. *Environmental Science & Technology* 51.

Swart PK, Greer L, Rosenheim BE, et al. (2010) The 13C Suess effect in scleractinian corals mirror changes in the anthropogenic CO2 inventory of the surface oceans. *Geophysical Research Letters* 37(5): L05604.

Thompson R and Oldfield F (1986) *Environmental magnetism.* Allen & Unwin, London.

Tylmann W, Fischer HW, Enters D, et al. (2014) Reply to the comment by F. Gharbi on" Multiple dating of varved sediments from Lake Łazduny, northern Poland: Toward an improved chronology for the last 150 years". *Quaternary Geochronology* 20: 111-113.

UNSCEAR (2000) *Sources and effects of ionizing radiation, United Nations scientific committee on the effects of atomic radiation (UNSCEAR) 2000 report.* New York: United Nations.

Wang Y, Sheng HF, He Y, et al. (2012) Comparison of the levels of bacterial diversity in freshwater, intertidal wetland, and marine sediments by using millions of illumina tags. *Applied and Environmental Microbiology* 78(23): 8264-8271.

Waters CN, Turner SD, Zalasiewicz J, et al. (2022) Candidate sites and other reference sections for the Global boundary Stratotype Section and Point (GSSP) of the Anthropocene Series. *The Anthropocene Review*. Submitted.

Waters CN, Zalasiewicz J, Summerhayes C, et al. (2018) Global Boundary Stratotype Section and Point (GSSP) for the Anthropocene Series: Where and how to look for potential candidates. *Earth-Science Reviews* 178: 379-429.

Wen T (2012) *Eight crises:Lessons from China, 1949-2009.* Beijing, China: Dongfang Press.

Wieland E, Santschi PH, Höhener P, et al. (1993) Scavenging of Chernobyl ^{137}Cs and natural ^{210}Pb in Lake Sempach, Switzerland. *Geochimica Et Cosmochimica Acta* 57(13): 2959-2979.

Wolfe AP, Hobbs WO, Birks HH, et al. (2013) Stratigraphic expressions of the Holocene–Anthropocene transition revealed in sediments from remote lakes. *Earth-Science Reviews* 116: 17-34.

Wu F, Zheng J, Liao H, et al. (2010) Vertical distributions of plutonium and ^{137}Cs in lacustrine sediments in northwestern china: quantifying sediment accumulation rates and source identifications. *Environmental Science & Technology* 44(8): 2911-2917.

Xing S, Zhang W, Qiao J, et al. (2018) Determination of ultra-low level plutonium isotopes (Pu-239,240) in environmental samples with high uranium. *Talanta* 187: 357-364.

Xu HM, Cao JJ, Ho KF, et al. (2012) Lead concentrations in fine particulate matter after the phasing out of leaded gasoline in Xi'an, China. *Atmospheric Environment* 46: 217-224.

Yan D, Xu H, Lan J, et al. (2020) Warming favors subtropical lake cyanobacterial biomass increasing. *Science of the Total Environment* 726: 138606.

Zalasiewicz J, Waters CN, Summerhayes CP, et al. (2017) The Working Group on the Anthropocene: Summary of evidence and interim recommendations. *Anthropocene* 19: 55-60.

Żarczyński M, Tylmann W and Goslar T (2018) Multiple varve chronologies for the last 2000 years from the sediments of Lake Żabińskie (northeastern Poland) – Comparison of strategies for varve counting and uncertainty estimations. *Quaternary Geochronology* 47.

Zhang J, Li J, Yan Y, et al. (2019a) A 1000-year record of centennial-scale cyclical vegetation change from Maar Lake Sanjiaolongwan in northeastern China. *Journal of Asian Earth Sciences* 176: 315-324.

Zhang L, Hou X, Li H-C, et al. (2018) A 60-year record of I-129 in Taal Lake sediments (Philippines): Influence of human nuclear activities at low latitude regions. *Chemosphere* 193: 1149-1156.

Zhang Q, Zheng Y, Tong D, et al. (2019b) Drivers of improved PM2.5 air quality in China from 2013 to 2017. *Proceedings of the National Academy of Sciences of the United States of America* 116(49): 24463-24469.

Zhao X, Hou X and Zhou W (2019) Atmospheric iodine (^{127}I and ^{129}I) record in spruce tree rings in the Northeast Qinghai-Tibet Plateau. *Environmental Science & Technology* 53(15): 8706-8714.

Zhuang Q, Li G, Wang F, et al. (2019) 137Cs and 239+240Pu in the Bohai Sea of China: Comparison in distribution and source identification between the inner bay and the tidal flat. *Marine Pollution Bulletin* 138: 604-617.

Supplementary data

Note: The text has supplementary information including (1) Analytical methods for the Anthropocene proxy measurements; (2) Figures S1-S6; (3) Table S1-S2; and (4) SI references.

Acknowledgements

Analysis of the Sihailongwan maar Lake cores was facilitated by the collaborative research project between the Anthropocene group of the IEECAS and the AWG to ratify the stratigraphic Anthropocene. The AWG is co-ordinating the assessment of candidate GSSP sites in collaboration with the Haus der Kulturen der Welt (HKW, Berlin) in the framework of its long-term project Anthropocene Curriculum. The Anthropocene Curriculum is an international project for experimental forms of Anthropocene research and education developed by HKW and the Max Planck Institute for the History of Science (MPIWG, Berlin) since 2013. The authors are sincerely grateful to Prof. Colin N. Waters of University of Leicester and Dr. Simon D. Turner of University College London for their valuable guidance and constructive comments on our GSSP work. Also, many thanks to Dr. George S. Burr for his careful editing and valuable comments.

Funding

This work was supported by the National Natural Science Foundation of China [41991250, 42221003, and 41625015], the Strategic Priority Research Program of CAS [XDB40000000], and Haus der Kulturen der Welt funding.

Supplementary information for

The Sihailongwan maar Lake, northeastern China as a candidate Global Boundary Stratotype Section and Point for the Anthropocene Series

The PDF includes:

Analytical methods for the Anthropocene proxy measurements;

Figures S1-S6;

Tables S1-S2;

SI references.

Analytical methods for the Anthropocene proxy measurements

Lithology

Grayscale analyses and Photography Grayscale data were obtained using digital image processing. After a photographic image of the frozen core section was taken from core SHLW21-Fr-13, a strip of the image without pores and cracks was analyzed. The grayscale values of the strip (lightness and darkness) under direct light irradiation, was extracted using MATLAB software (MathWorks company, USA). The grayscale range was 0 to 255, with 0 representing black and 255 indicating white.

In addition, a strip (20 × 2 × 2 cm) was cut off from the frozen core (SHLW21-Fr-13) with a knife, and the surface of the spline was carefully smoothed to reduce scanning errors caused by core slicing irregularities. The spline surface was subsequently covered with a thin (4 μm) Ultralene® film, which further diminished surface roughness, minimized desiccation, and prevented contamination of the X-ray fluorescence (XRF) spectrometer. An XRF Core Scanner (Avaatech, the Netherlands), recorded images and colors of the strip using visible and ultraviolet light with cross core coverage up to 1600 mm long, 140 mm wide (maximum dimensions of core sample) and 42 μm resolution. The Avaatech line scan software produces visual color images and RGB and CIELAB color data.

Core Scanning and Dry Bulk Density (DBD) Analysis The strip (20 × 2 × 2 cm of core SHLW21-Fr-13) was next placed in an aluminium box (22 × 3 × 2.5 cm), freeze-dried, and impregnated in a mixture of epoxy resin (epoxy resin-128, Yueyang Petrochemical) and triethanolamine (Macklin) in a mass ratio of 8:1. The impregnated strip was hardened in an oven at 50°C for 24 hours and then polished with 30, 10, 5, 1 micron sandpaper in sequence on a grinder and polisher. The polished core strip was scanned at 0.1-cm resolution using an Avaatech XRF core scanner (Avaatech, the Netherlands) at the Institute of Earth Environment, Chinese Academy of Sciences (IEECAS). Ten elements (Al, Si, P, S, Cl, K, Ca, Ti, Mn, and Fe) were measured at an X-ray voltage of 10 kV; 10 elements (Cu, Zn, Ga, As, Br, Rb, Sr, Y, Zr, and Mo) were measured at 30 kV, and 11 elements (Ru, Pd, Ag, Cd, In, Sn, Sb, Te, I, Cs and Ba) were

measured at 50 kV (Richter and Howard, 2000; Tjallingii et al., 2007).

A strip (~20 × 2 × 2 cm) was cut from the freeze core SHLW21-Fr-13 and refined into a standard cube in the Sediment Core Repository room of the IEECAS. It was then subsampled carefully at 0.2 cm intervals along the varve direction in the freeze cores. The subsamples were freeze dried and weighed with a balance. The bulk density of each sample was calculated according to its volume.

Magnetic Susceptibility (MS) MS is a measure of the degree to which minerals become magnetized in an applied magnetic field. MS values range from negative to highly positive (Dearing et al., 1996). The subsamples (~0.2 g) of core SHLW21-Fr-9 were ground into powder (<63 μm) and freeze-dried. Low-frequency (470 Hz) and high-frequency (4700 Hz) magnetic susceptibilities were measured using a MS meter (Bartington, model MS2, UK) at the Environmental Magnetism Laboratory in the IEECAS (Dearing et al.1996).

Radioisotopes

Plutonium Two plutonium isotopes (^{239}Pu, ^{240}Pu) were determined using a procedure modified from Qiao et al. (2009). An aliquot of ~0.5 g sediment from core SHLW21-Fr-13 was weighed into a beaker and ashed in a muffle furnace at 450ºC for 12 h to decompose organic matter. A 1 mBq ^{242}Pu spike was added as a tracer to monitor the chemical yield of plutonium for the separation procedure. *Aqua regia* was used to digest the samples and to leach the plutonium from sediment particles. Ammonia was added to the leachate to co-precipitate plutonium with $Fe(OH)_3$ at pH = 8–9. Then the precipitate was dissolved with concentrated HCl, and plutonium isotopes were converted into Pu^{3+} by addition of $K_2S_2O_5$. The precipitate was again adjusted to pH 9 to 10 with ammonia. The precipitate was separated and dissolved in concentrated HCl, and concentrated HNO_3 was added to oxidize Pu^{3+} to Pu^{4+}. The samples were immersed in a 3 M HNO_3 solution and loaded into a TEVA (teva resin) column (2 mL) (TRISKEM, Bruz, France). After rinsing with 120 mL 3 M HNO_3 and 60 mL 6 M HCl to remove interfering elements (U and Th), Pu on the column was finally eluted with 40 mL of a 0.1 M $NH_2OH{\cdot}HCl$-2M HCl solution. The eluate was evaporated to dryness,

a few drops of concentrated HNO_3 were added, and then it was evaporated to dryness again to decompose the hydroxylamine and remove the remaining HCl. The residue was dissolved in 0.5 M HNO_3. One procedural blank sample was prepared for each 7 samples using the same procedures as above for quality control.

^{239}Pu, ^{240}Pu, and ^{242}Pu in the sample solution were measured using a triple quadrupole ICP-MS (Agilent 8800 ICP-MS/MS, Agilent Technologies, Tokyo, Japan) with a NH_3-He mixture as the reaction gas. Details concerning the measurement methods have been reported elsewhere (Xing et al., 2018). The detection limits of this method for ^{239}Pu and ^{240}Pu are estimated to be 0.55 and 0.09 fg mL^{-1}, respectively, using 3 times standard division of the count rates of the procedural blanks and the measured sensitivity of instrument for plutonium isotopes. The measured count rates for ^{239}Pu and ^{240}Pu in the procedural blanks were 0.55 and 0.04 counts per second (cps), respectively, which are 1 to 3 orders of magnitudes lower than that in the samples.

The instrumental background was assessed using 0.5 M HNO_3, and the measured ^{238}U and ^{239}Pu count rates were 3.00 and 0.10 cps, which were at least 1 to 2 orders of magnitude lower than those in the procedural blanks or samples. ^{242}Pu was added to the samples before separation, and they were both used as isotope dilution standards to calculate ^{239}Pu and ^{240}Pu concentrations in the samples and to estimate the plutonium recoveries for the chemical separation (most were >75%). The low instrumental background and low procedural blanks, as well as the high chemical yield together ensure the reliability of the analytical results of ^{239}Pu and ^{240}Pu.

Iodine The detailed analytical procedure for determination of iodine isotopes in sediment samples have been reported previously (Zhang et al., 2018; Zhang et al., 2011). These consist of pyrolysis/combustion separation, solvent extraction purification, and mass spectrometric measurement. The SHLW21-Fr-7 core samples were weighed (0.2-2 g), spiked with ^{125}I as a chemical yield tracer, and placed into a four-tube pyrolyser furnace (Prolyser-4 Trio^{TM}, Raddec LTD., UK) for iodine separation. Iodine isotopes were oxidized by O_2 to gaseous molecular iodine (I_2) at 800℃, carried by O_2/N_2 flow and trapped into an alkaline trapping solution. Two aliquots of the trapping solution were reserved for ^{127}I determination by ICP-MS (Agilent 8800, USA), and for ^{125}I

counting using a NaI gamma counter (FM-1000, Xi 'an Kaipu Electromechanical Co. LTD) to calculate chemical yields during pyrolysis.

The remaining solution was used for ^{129}I determinations. Solvent extraction was adopted for iodine purification from trapping solutions. The trap solutions were spiked with ^{127}I carrier (Woodward corporation, USA), iodine species were converted to iodide with $NaHSO_3$, and adjusted to pH < 2 with HNO_3. Iodine in the solution was extracted with CCl_4 after addition of $NaNO_2$ to oxidize iodide to I_2. After separation from the water phase, iodine in the CCl_4 was back extracted using H_2O with addition of $NaHSO_3$ to reduce I_2 to iodide. After further purification by repeating the CCl_4 extraction and $NaHSO_3$ back extraction, the separated iodine (^{129}I, ^{127}I and ^{125}I) was transferred to a centrifuge tube, then $AgNO_3$ solution was added to precipitate AgI. The AgI precipitate was washed with HNO_3 and deionized water, dried, mixed with niobium powder and pressed into a copper holder. ^{129}I in the prepared target was measured by AMS (3 MV, HVEE, the Netherlands) in the Xi'an AMS Center (Hou et al., 2010).

Blank samples were prepared using the same procedure without addition of soils and sediments.$^{129}I/^{127}I$ ratios of the instrumental blanks were about 2×10^{-13}, and the analytical precisions were within 5% for all samples. The instrumental detection limit of ^{127}I is 0.002 μg L^{-1}.

Soot radiocarbon The method used for soot radiocarbon analyses has been described in detail in Han et al. (2022). Briefly, sediment samples (~0.1 g) taken from core SHLW21-Fr-1 were pretreated with acid to remove carbonate, minerals and oxides, and then filtered using pre-fired quartz filters. A combustion protocol with three temperature steps was used to isolate the soot carbon fractions. The procedure was based on methods described and tested in Dusek et al. (2014), and the samples were analysed using an Automated Aerosol Combustion (AAC) system described in Dusek et al. (2019). CO_2 resulting from the combustion of soot was recovered and stored in flame-sealed glass vials until ^{14}C analysis.

Radiocarbon analyses were performed using the gas inlet system (Dusek et al., 2019) of the Mini Carbon Dating System accelerator mass spectrometer (AMS) (Ruff et al., 2007) at the Centre for Isotope Research in the Energy and Sustainability

Research Institute Groningen, the Netherlands. The $F^{14}C$ values were corrected for memory effects and instrument background (Synal et al., 2007; Wacker et al., 2010), and they were normalized to the average value of gaseous OXII (an oxalic acid) standards. Contamination introduced during sample handling and the combustion steps was ~0.97 ± 0.14 μg C with an average $F^{14}C$ of 51 ± 15%. The contamination was quantified and corrected for as described in Dusek et al. (2019). Following Han et al. (2022), the fossil fuel fraction calculations were based on the measured $F^{14}C$ values and assuming that biomass soot in Sihailongwan sediments originated mainly from the burning of 50% 50 year-old trees and 50% crops.

Novel materials

Spheroidal carbonaceous particles (SCPs) Sediment samples collected from core SHLW21-Fr-1 were analysed for SCPs following the method described by Rose (1994) in the Department of Geography, University College London. Dried sediment (~0.1 g) was subjected to sequential chemical attack by mineral acids to remove unwanted fractions leaving a suspension of mainly carbonaceous material and a few resistant minerals. SCPs are mostly composed of elemental carbon particles, which are chemically refractory. The use of concentrated nitric acid (to remove organic material), hydrofluoric acid (siliceous material) and hydrochloric acid (carbonates and bicarbonates) therefore does them no damage. A known fraction of the final suspension was transferred to a coverslip, evaporated, and mounted onto a microscope slide. The numbers of SCPs on the coverslips were counted using a light microscope at 400× magnification, and the sediment concentration was calculated as the number of particles per gram dry mass of sediment (gDM^{-1}).

The SCP identification criteria under a microscope followed the procedure of Rose (2008). The detection limit for the technique is typically ~100 gDM^{-1} and concentrations have an accuracy of approximately ± 45 gDM^{-1} (Rose 2008). SCP counts were sub-divided into size classes whilst counting. Analytical blanks were analysed in duplicate as was an SCP reference material. Reference concentrations agreed closely with expected values (6005 ±70 gDM^{-1}), and no SCPs were observed in the blanks.

Polycyclic aromatic hydrocarbons (PAHs) A detailed description of PAH analyses has been reported previously (Bandowe et al., 2010; Han et al., 2015; Wei et al., 2015). Approximately 0.5 g of sediment was subsampled from gravity core SHLW20-6 and then weighed (1/10,000 balance), spiked with an internal standard (20 ng/μL, 25 μL), wrapped by a clean filter, and extracted ultrasonically with dichloromethane (20 mL), acetone:dichloromethane:TFA (trifluoroacetic acid) (250:125:1 v/v/v, 20 mL) and dichloromethane (20 mL) stepwise for three times (15 minutes each). Ice was used to prevent evaporation during the extraction, and the extracts were collected and combined after three extractions. The combined extracts were concentrated, solvent-exchanged into hexane, and then reduced to ~1 mL by a rotary evaporator. The extracts were cleaned through 3 g of silica gel (10% deactivated) in 8 mL borosilicate glass columns (J.T. Baker, USA). PAHs were eluted with 15 mL of hexane–dichloromethane mixture (5:1, v/v). The eluents were concentrated again, exchanged into hexane, and then transferred to 1 mL sample vials.

The samples were analyzed by an Agilent gas chromatograph (7890B)/mass spectrometer (5977A) (GC/MS). The GC was equipped with an HP-5MS column (5% phenyl-95% methyl-polysiloxane, 30 m long × 0.25 mm diameter × 0.25 μm film thickness). The column oven temperature was initially held at 60°C for 5 min, and then increased to 290°C at a rate of 3°C min^{-1} and held for 15 min. The injector temperature was kept at 280°C and purified helium (99.9999%) was used as the carrier gas and delivered at a constant flow rate of 1 mL min^{-1}.

In total, 26 PAH species were measured in this study, including 1,2,3,4-tetrahydronapthalene, naphthalene, 2-methylnaphthalene, 1-methylnaphthalene, 1,3-dimethylnaphthalene, acenaphthylene, acenaphthene, fluorene, phenanthrene, anthracene, 2-methylphenanthrene, 3,6-dimethylphenanthrene, fluoranthene, pyrene, retene, benzo(a)anthracene, chrysene, benzo(b)fluoranthene, benzo(j)fluoranthene, benzo(k)fluoranthene, perylene, benzo(e)pyrene, benzo(a)pyrene, indeno(1,2,3-cd)pyrene, Dibenzo(a,h)anthracene, and benzo(ghi)perylene. The parent (unsubstituted) PAHs are the sum of naphthalene, acenaphthylene, acenaphthene, fluorene, phenanthrene, anthracene, fluoranthene, pyrene, benzo(a)anthracene, chrysene,

benzo(bjk)fluoranthene, benzo(e)pyrene, benzo(a)pyrene, indeno (1,2,3-cd)pyrene, dibenzo(a,h)anthracene, and benzo(ghi)perylene. High molecular wight (HMW-) PAHs are the sum of 4-7 ring species, including fluoranthene, pyrene, benzo(a)anthracene, chrysene, benzo(bjk)fluoranthene, benzo(e)pyrene, benzo(a)pyrene, indeno(1,2,3-cd)pyrene, dibenzo(a,h)anthracene, and benzo(ghi)perylene, while low molecular weight (LMW-) PAHs are 2-3 ring species, including naphthalene, acenaphthylene, acenaphthene, fluorene, and phenanthrene.

Black carbon, char, and soot BC, char and soot analyses were conducted using the thermal/optical IMPROVE method, which has been described in detail in several publications (Han et al., 2009; Han et al., 2007a; Han et al., 2007b; Han et al., 2011). In brief, ~0.1 g of dried powdered samples (less than 63 μm) collected from core SHLW21-Fr-1 were acid-pretreated to remove carbonates, minerals, and oxides etc., and the residues were then filtered using pre-fired, 47 mm diameter quartz filters to remove any remaining carbon. Then, small punches (0.526 cm^2) of the filters were heated in a stepwise process in inert and oxidized atmospheres using a commercial organic carbon/elemental carbon (OCEC) instrument (DRI model 2001A, Atmoslytic, USA). Four organic carbon fractions (OC1, OC2, OC3, and OC4); three elemental carbon fractions (EC1, EC2, and EC3); and a pyrolyzed organic carbon fraction (POC), were determined with the use of a laser installed in the OCEC instrument. BC was calculated as the sum of all EC fractions minus POC (Chow et al., 1993), while char and soot were defined as EC1 minus POC and the sum of EC2 and EC3, respectively (Han et al., 2007a).

Organic matter and their stable isotopes

Organic matter The organic matter (total organic carbon, TOC, and total nitrogen, TN) concentrations were determined using DIN-19539 method (2015) using a Soli TOC cube Analyzer (Elementar, Germany). For these analyses, ~0.2 g of the dried and ground samples collected from core SHLW21-Fr-2 were weighed and then heated to temperatures of 400, 600, and 900°C, at which total organic carbon (TOC), residual oxidizable carbon (ROC), and inorganic carbon (IC), respectively, were combusted.

Meanwhile, organic nitrogen also was measured in this process.

TOC stable carbon isotopes TOC stable isotope ($\delta^{13}C$) analysis involved the following three steps: sample pretreatment, generation of CO_2, and mass spectrometric analysis. These methods have been described in detail in Cao and Liu (2011). In brief, ~0.2 g subsamples of core SHLW21-Fr-2 were taken and hydrochloric acid was added to remove carbonate. The samples were washed (to near neutral pH), dried, ground, and stored in a pretreated glass vial. The pretreated samples were then put into quartz tubes; copper oxide, copper wire and platinum wire were added; and the tubes were vacuum sealed. The sealed tubes were then put into a muffle furnace at 850°C for at least 2.5 h to ensure the complete oxidation of organic matter. Then the samples were placed on a CO_2 gas purification device which used liquid nitrogen to remove any water, and the pure CO_2 gas was collected. Carbon isotopes were determined at the Stable Isotope Biogeochemistry Laboratory at the IEECAS using a MAT 251 isotope ratio mass spectrometer (IRMS, Finnigan MAT 251). National reference material GBW04407 (carbon black) was analyzed to monitor the sample preparation process and the performance of the mass spectrometer.

Nitrogen stable isotopes Each sediment sample (~0.2 g) from core SHLW21-Fr-2 was freeze-dried and ground using a mortar and pestle. The samples were sieved through a 63 μm screen and preserved. The nitrogen isotope ratios ($\delta^{15}N$) were determined at the Stable Isotope Biogeochemistry Laboratory at the IEECAS using an elemental analyzer (model: FLASH EA1112 SERIES and manufacturer information: CE INSTRUMENTS) interfaced to continuous-flow isotope ratio mass spectrometer (IRMS, model: Delta Plus and manufacturer information: Thermo Finnigan) (Liu et al., 2011). All $\delta^{15}N$ values were reported relative to an atmospheric N_2 standard. An international isotope reference material (IAEA-N3; $\delta^{15}N$= 4.70‰) and a soil standard with a known $\delta^{15}N$ value were measured each day to monitor the analytical accuracy of the EA-IRMS. The standard deviation for repeated sample analyses was less than 0.3‰.

Inorganic geochemical elements

Inorganic elements Approximately 0.1 g of each sample collected from core

SHLW21-Fr-9 was digested with 2 mL 49% HF and 6 mL 68% HNO_3 in a Teflon® bomb in a microwave digestion instrument (M3, PreeKem Scientific Instruments Co., Ltd, Shanghai, China). After evaporation to dryness, 1 mL 70% $HClO_4$ was added to the residue and again heated at about 170℃ until the mixture was evaporated to 0.5 to 1 mL, then diluted to 10 mL with ultrapure water.

Inorganic element concentrations were determined by a microwave plasma atomic emission spectrometer (4200 MP-AES, Agilent Technologies, Santa Clara, CA, USA). With this instrument, Zn, Cd, Cu, Pb and Cr could be measured directly, but K, Ca, Na, Mg, Fe and Mn had to be diluted 20-fold before measurement due to their high concentrations. To test the analytical accuracy and precision of the results, duplicate sample analyses were performed for 10% of all samples; this quality control step was used to verify the stability of the instrument and provide a measure of the reproducibility. The analytical precision was estimated to be <5%. The averages of the replicate analyses were within the analytical errors of the reference values.

Hg and Hg isotopes Sediment samples from core SHLW21-Fr-2 were freeze-dried, milled to 100 mesh size, and kept frozen until Hg and Hg isotope analyses. Approximately 30 ± 5 mg of each sample was weighed and loaded into a DMA-80 automatic mercury analyzer (Milestone Srl., Italy), and Hg concentrations were measured automatically (Fu et al., 2014). The performance of the DMA-80 Hg analyzer was verified every five samples using a standard reference material (NIST SRM 2711a, Montana II soil). For the Hg isotope ratio determinations, Hg in the sediments (100–200 mg) was desorbed using a two-stage offline combustion protocol. That process releases elemental Hg which was subsequently trapped in 5 mL 40% mixed acid solution (v/v: $2HNO_3$/1HCl) (Fu et al., 2014; Biswas et al., 2008). The trap solution was diluted to a Hg concentration of 0.5 or 1.0 ng mL^{-1} for Hg isotope ratio analysis. Hg isotope ratios were determined by cold vapor-multicollector inductively coupled plasma mass spectrometry (CV-MC-ICPMS, Nu Instruments, U.K.) (Fu et al., 2019). The isotope ratios for Hg in the sediments were reported in delta notation (δ in ‰) referenced to the NIST SRM 3133 standard (Blum and Bergquist, 2007):

$$\delta^{202}\mathrm{Hg}(‰)=\left(\frac{\left(^{202}\mathrm{Hg}/^{198}\mathrm{Hg}\right)_{\mathrm{sample}}}{\left(^{202}\mathrm{Hg}/^{198}\mathrm{Hg}\right)_{\mathrm{NIST\text{-}3133}}}-1\right)\times 1000 \quad (1)$$

MIF values (mass independent fractionation, Δ^{xxx}Hg) were calculated for ^{xxx}Hg isotopes using the following equation:

$$\Delta^{xxx}\mathrm{Hg}=\delta^{xxx}\mathrm{Hg}-\beta_{xxx}\cdot\delta^{202}\mathrm{Hg} \quad (2)$$

where *xxx* represents mass numbers 199, 200 and 201 with corresponding scaling factors β_{xxx} of 0.2520, 0.5024 and 0.7520.

The QA/QC for the isotopic composition analyses involved routine measurements of NIST RM 8610 (UM-Almaden Mono-elemental Secondary standard solution). The mean δ^{202}Hg, Δ^{199}Hg, and Δ^{200}Hg values of NIST RM 8610 (n = 12) measured in this study were -0.52 ± 0.07‰, -0.03 ± 0.06‰, and 0.02 ± 0.06‰, respectively. These agree with values reported previously (Blum and Johnson, 2017). The analytical (2 standard deviation, sd) uncertainty of the Hg isotopic composition was calculated as the larger of 2 times the standard deviation value of either NIST SRM 8610 or the replicate analyses of the samples.

Biotic markers - eDNA

Total genomic DNA was extracted from two subsamples of 0.5 g wet sediments collected from core SHLW21-Fr-14 using the Fast DNA SPIN Kit for soil (MP Biomedical, USA) following the manufacturer's instructions (Yan et al., 2020). Then, DNA extracts of the two subsamples were pooled together and the concentrations of total DNA extracts were quantified using a Quibt3.0 Flex fluorometer (Life Invitrogen, USA). Further, the 23S rRNA gene was amplified by polymerase chain reaction (PCR) using the algae-specific primer pairs p23SrV_f1-GGACAGAAAGACCCTATGAA and p23SrV_r1-TCAGCCTGTTATCCCTAGA (Sherwood and Presting, 2007) to investigate the diversity and community structure of phytoplankton. Each PCR amplification including negative controls was conducted in a 25 μL reaction system containing 1 μL of DNA template, 0.4 μL of each primer, 2.5 μL of 10×Ex Taq Buffer, 2 μL of 2.5 mM dNTPs, 0.25 μL of Ex Taq Polymerase (Takara, Japan) and 18.45 μL

aseptic water. The PCR amplification was performed on an ABI GeneAmp® 9700 PCR System (USA) under the following conditions: an initial denaturation at 98°C for 10 s, 30 cycles of 30 s at 55°C, 1 min at 72°C, and a final extension at 72°C for 10 min. PCR was replicated in triplicate and the products of each sample were pooled. Finally, the PCR products were purified using a MiniBEST Agarose Gel DNA Extraction Kit (Takara, Japan), and the purified PCR products from 51 samples were mixed in equal amounts and subjected to Illumina Miseq sequencing at Shanghai Personalbio Technology Co Ltd (Shanghai, China).

The raw sequence data were analyzed using the Quantitative Insights Into Microbial Ecology (Qiime) open source platform. The barcodes, primer sequences, and the low-quality sequences were removed using USEARCH software (Edgar et al., 2011), thus providing effective sequences for the subsequent analyses. Thereafter, the effective sequences were grouped into Operational Taxonomic Units (OTUs) at 97% similarity levels. The taxonomic identities of those OTUs were assigned using the NCBI database (https://www.ncbi.nlm.nih.gov) at the 80% confidence threshold (Yan et al., 2019). Further, the alpha diversity Shannon index that is commonly used to reflect the phytoplankton diversity (Wang et al., 2012) was calculated using Python script (*alpha_diversity.py*). In order to compare the phytoplankton beta diversity between different sediment layers, principal component analysis (PCA) was performed on the relative sequence abundance data at the OTU level using Python script (*beta_diversity.py*), and then the PC1 component, which is used to show the major temporal change pattern of the community structure, was extracted from the PCA analysis. Then, the PC1 scores were plotted against age to detect tipping points of the phytoplankton structure (Figure 8 in the main text).

After the filtering and processing steps of the raw sequence data, 2,550,000 reads in total were clustered into 5565 OTUs at the 97% identity level, and the OTUs were classified into 17 groups at the 2end rand (phylum level), 39 groups at the 3rd rank (class level), 107 groups at the 5th rank (family level), 235 groups at the 6th rank (genus level). Cyanobacteria, Chrysophyceae, Rhodophyta, Chlorophyta, Dinophyta, Cryptophyta, Bacillariophyta, Eustigmatophyta were the dominant group at the phylum

level. The dominant families including *Synechococcaceae*, *Chromulinaaceae*, *Bangiaceae*, *Rivulariaceae*, *Rhodochaetaceae*, *Gloeobacteraceae*, *Chlamydomonadaceae*, *Haematococcaceae*, *Dinophysiaceae* were identified. The dominant species including *Chromulina sp. SAG 17.97*, *Synechococcus rubescens*, *Chlamydomonas noctigama*, *Choricystis parasitica*, *Cyanobium gracile*, *Scherffelia dubia*, *Bacillus subtilis*, *Chrysosporum ovalisporum*, *Ochromonas sp. SAG 933.10*, *Cyanobium sp. PCC 7009* were also identified and analyzed. Details are shown in Supplement Table S2.

Figure S1. Sihailongwan maar Lake in Jilin Province, NE China. Photograph courtesy of Mr. Pengfei Ji at Jilin TV Station.

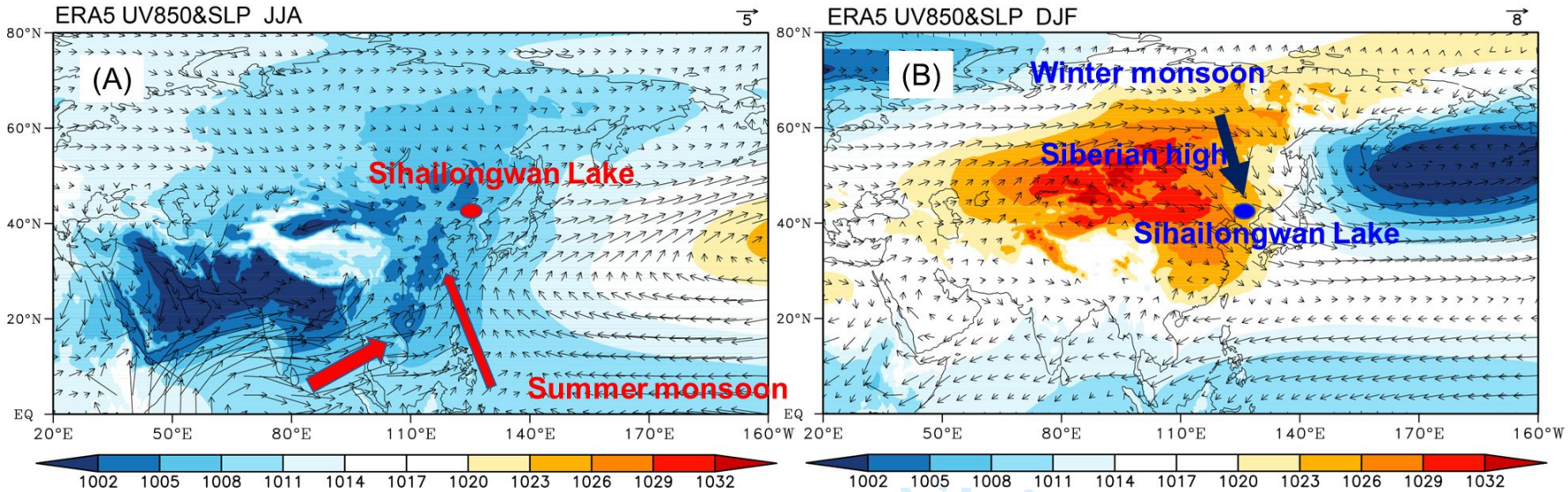

Figure S2. Annual average (A) winter and (B) summer mean sea level pressure and 850 hPa horizontal wind field (1979–2019 CE) according to ERA5 re-analysis data.

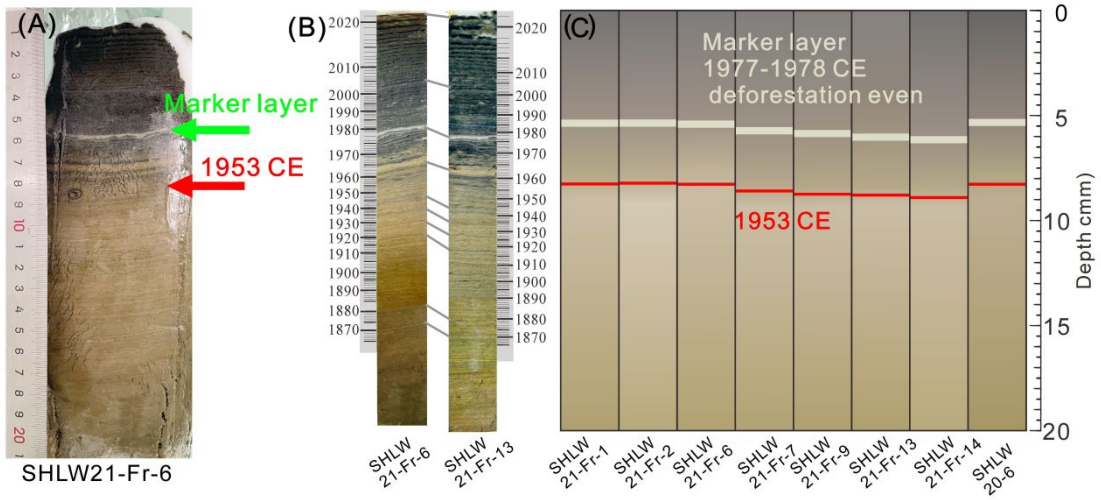

Figure S3. Lithology of the different sediment cores of the Sihailongwan Lake. (A) Photograph of the varve layers of the SHLW21-Fr-6 freeze core. (B) Core-to-core comparison of varves between cores SHLW21-Fr-13 and SHLW21-Fr-6, which shows a dated stratigraphic comparison between different cores. The lines between the two cores indicate similar varves in the two cores (C) Sketch map of the locations of the siliciclastic marker layer (corresponding to 1977-78 CE) and 1953 CE in different sediment cores. The upper sections of all the cores record a marker layer from 1977-78 CE caused by deforestation. The anthropogenic proxies measured in this study are all from these cores.

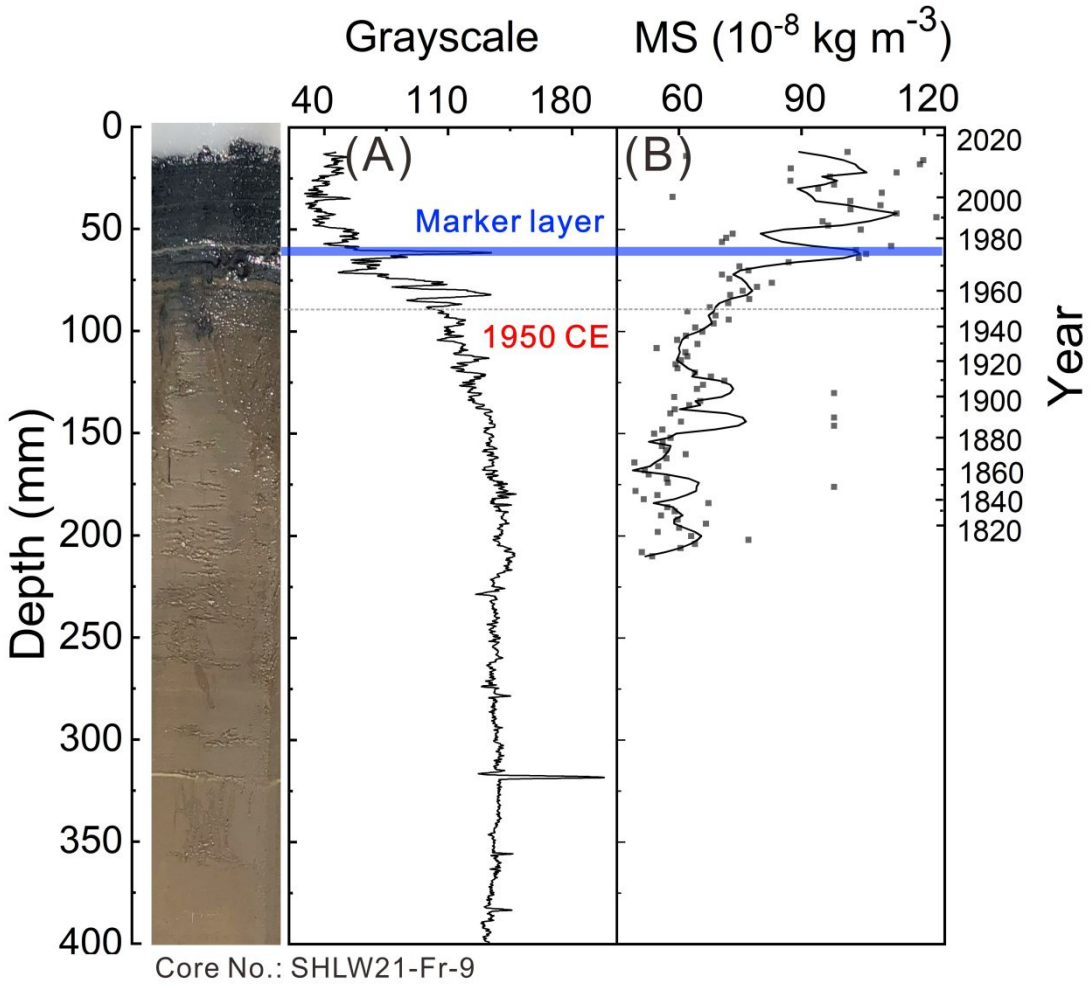

Figure S4. Photograph, grayscale and magnetic susceptibility (MS) results of sediment core SHLW21-Fr-9.

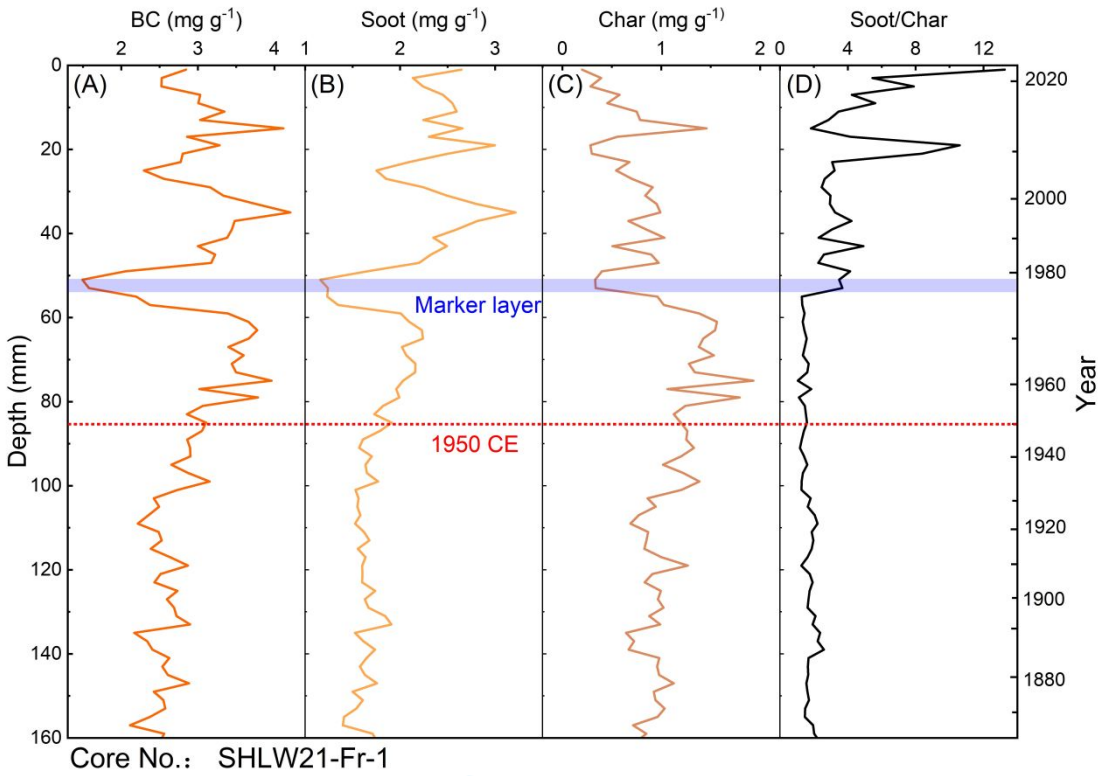

Figure S5. Historical variations of (A) black carbon (BC), (B) soot, and (C) char concentrations and (D) soot/char ratio versus depth and age in core SHLW21-Fr-1 from Sihailongwan Lake. The shaded region highlights the siliciclastic marker layer that occurred around 1977–78 CE due to the deforestation activities that led to increased inputs of detrital material.

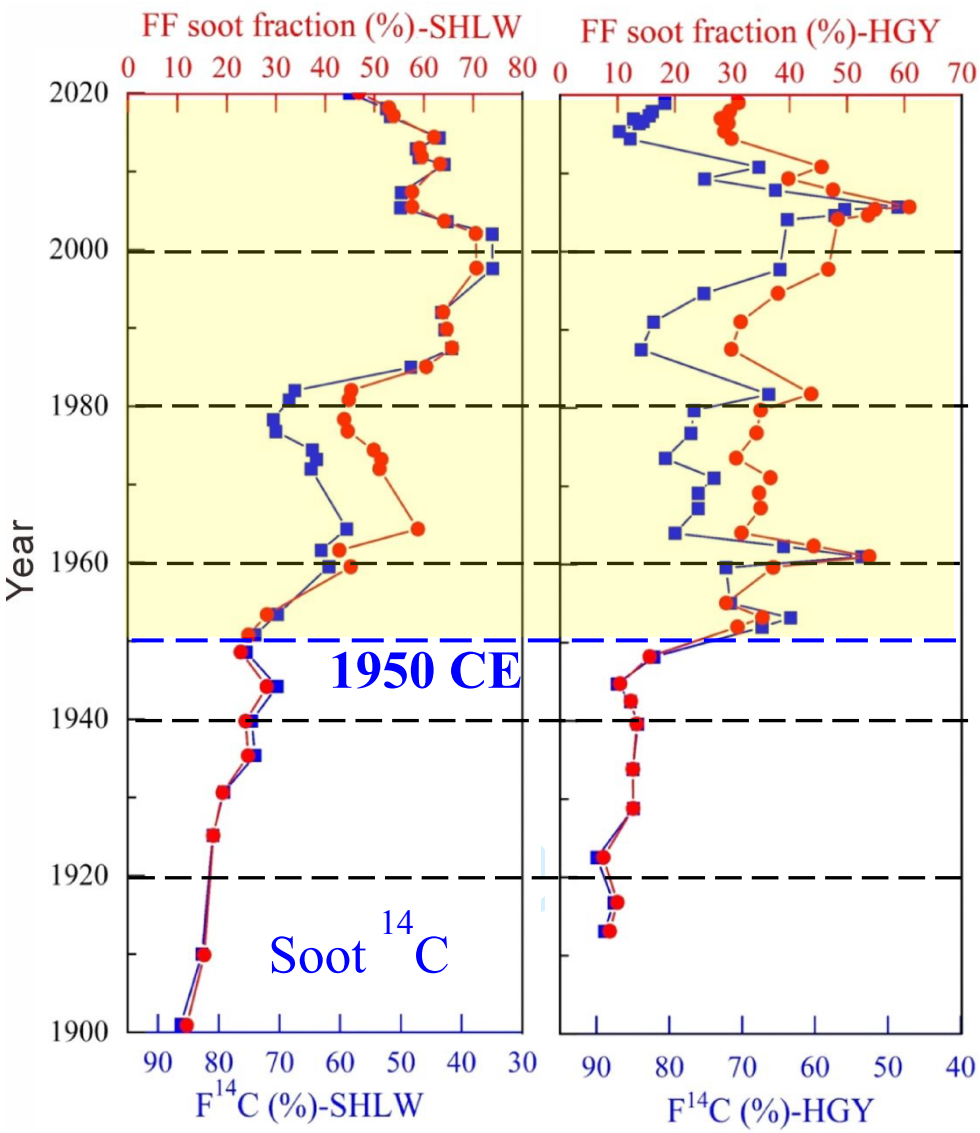

Figure S6. Comparison of soot ^{14}C (blue) and fossil fuel (FF) soot fractions (red) in Sihailongwan (SHLW) and Huguangyan (HGY) maar Lakes, which are over 2,000 km apart.

Table S1. Proxy measurements with corresponding core number, number of samples, and sample resolution, also for period 1935-1965 CE in Sihailongwan maar Lake. Note: on average, 1 mm represents a time period of ~1 yr. For PAHs, only 150 mm length from the upper part of gravity core SHLW20-6 were measured.

Proxies	Core No.	Number of samples	Sample resolution (mm)	Sample resolution for period 1935-1965 CE (mm)
MS	SHLW21-Fr-9	100	2	2
^{210}Pb, ^{137}Cs	SHLW21-Fr-13	62	2-12	2
^{239,240}Pu	SHLW21-Fr-13	62	2-12	2
^{129}I	SHLW21-Fr-7	100	2	2
Soot ^{14}C	SHLW21-Fr-1	53	2-20	2-4
SCP	SHLW21-Fr-1	50	4	4
PAHs	SHLW20-6	60	2.5	2.5
Soot, char, and BC	SHLW21-Fr-1	100	2	2
TOC and TN	SHLW21-Fr-2	100	2	2
C, N isotope	SHLW21-Fr-2	91	2	2
Pb, Cu, Zn and Cd	SHLW21-Fr-9	100	2	2
Hg isotopes	SHLW21-Fr-2	50	4	4
eDNA	SHLW21-Fr-14	51	4	4

Table S2 Detailed description of the taxa measured in Sihailongwan maar Lake.

Phylum	Class	family
Cyanobacteria	*Chroococcales*	*Aphanothecaceae; Chroococcaceae; Cyanobacteriaceae; Microcystaceae*
	Chroococcidiopsidales	*Chroococcidiopsidaceae*
	Gloeobacteria	*Gloeobacteraceae*
	Gloeoemargaritales	*Gloeomargaritaceae*
	Nostocales	*Hapalosiphonaceae; Nostocaceae; Rivulariaceae; Scytonemataceae*
	Oscillatoriales	*Coleofasciculaceae; Cyanothecaceae; Gomontiellaceae; Microcoleaceae; Oscillatoriaceae*
	Pleurocapsales	*Dermocarpellaceae; Hyellaceae*
	Spirulinales	*Spirulinaceae*
	Synechococcales	*Acaryochloridaceae; Leptolyngbyaceae; Merismopediaceae; Oculatellaceae; Prochloraceae; Prochlorotrichaceae; Pseudanabaena; Schizotrichaceae; Synechococcaceae*
Bacillariophyta	*Bacillariophyceae*	*Bacillariaceae; Gomphonemataceae; Entomoneidaceae; Eunotiaceae; Phaeodactylaceae*
	Coscinodiscophyceae	*Melosiraceae; Thalassiosiraceae*
	Fragilariophyceae	*Licmophoraceae; Ulnariaceae*
	Mediophyceae	*Plagiogrammaceae*
Chrysophyceae	*Chrysophyceae*	*Plagiogrammaceae*
Cryptophyta	*Cryptomonadales*	*Cryptomonadaceae*
	Pyrenomonadales	*Geminigeraceae*
Dictyochophyceae	*Dictyochophyceae*	*Rhizochromulina*
Dinophyceae	*Dinophyceae*	*Dinophysiaceae; Gonyaulacaceae; Gymnodiniaceae; Lophodiniaceae; Kryptoperidiniaceae; Peridiniopsidaceae; Suessiaceae; Symbiodiniaceae; Thoracosphaeraceae*
Euglenida	*Euglenales*	*Euglenaceae; Phacaceae*
Eustigmatophyceae	*Eustigmatophyceae*	*Eustigmataceae; Monodopsidaceae; Trachydiscus*
Glaucocystophyceae	*Glaucocystophyceae*	*Glaucocystophyceae*
Haptophyceae	*Haptophyceae*	*Pavlovaceae; Phaeocystaceae; Chrysochromulinaceae*
Phaeophyceae;	*Phaeophyceae*	*Dictyotaceae; Dictyotaceae; Sargassaceae*
Raphidophyceae	*Raphidophyceae*	*Chattonellaceae*
Rhodophyta	*Bangiophyceae*	*Bangiaceae; Pyropia; Porphyridiaceae*
	Compsopogonophyceae	*Compsopogonaceae*
	Florideophyceae	*Acrochaetiaceae; Hapalidiaceae; Galaxauraceae; Nemastomataceae; Galaxauraceae; Rhodogorgonaceae; Lomentariaceae; Thoreaceae*
	Stylonematophyceae	*Stylonemataceae*
	Rhodellophyceae	*Dixoniellaceae*
Chlorophyta	*Chlorophyceae*	*Chaetophoraceae; Chlamydomonadaceae; Chlorococcaceae; Haematococcaceae; Chlorosarcina; Neochloridaceae; Scenedesmaceae; Selenastraceae*
	Chloropicophyceae	*Chloropicaceae*
	Mamiellophyceae	*Monomastigaceae*
	Pedinophyceae	*Resultomonadaceae; Pedinomonadaceae*
	Pyramimonadales	*Pyramimonadales*
	Trebouxiophyceae	*Chlorellaceae; Chlorellales*
	Ulvophyceae	*Pithophoraceae; Pseudoneochloris*
Viridiplantae	*unclassified Viridiplantae*	*unclassified Viridiplantae*
Xanthophyceae	*Xanthophyceae*	*Xanthophyceae*
unclassified	*unclassified*	*unclassified*

SI References:

Bandowe BAM, Shukurov N, Kersten M, et al. (2010) Polycyclic aromatic hydrocarbons (PAHs) and their oxygen-containing derivatives (OPAHs) in soils from the Angren industrial area, Uzbekistan. *Environmental Pollution* 158(9): 2888-2899.

Biswas A, Blum JD, Bergquist BA, et al. (2008) Natural mercury isotope variation in coal deposits and organic soils. *Environmental Science & Technology* 42(22): 8303-8309.

Blum JD and Bergquist BA (2007) Reporting of variations in the natural isotopic composition of mercury. *Analytical and Bioanalytical Chemistry* 388(2): 353-359.

Blum JD and Johnson MW (2017) Recent Developments in Mercury Stable Isotope Analysis. *Reviews in Mineralogy & Geochemistry* 82: 733-757.

Cao Y and Liu W (2011) Problems and improments of preparing organic carbon stable isotope samples by sealing tube method. *Journal of Earth Environment* 7: 200-208.

Chow JC, Watson JG, Pritchett LC, et al. (1993) The DRI thermal/optical reflectance carbon analysis system: description, evaluation and applications in U.S. Air quality studies. *Atmospheric Environment. Part A. General Topics* 27(8): 1185-1201.

Dearing JA, Dann RJL, Hay K, et al. (1996) Frequency-dependent susceptibility measurements of environmental materials. *Geophysical Journal International* 124(1): 228-240.

DIN-19539 (2015) Investigation of solids Temperature dependent differentiation of Total Carbon (TOC400, ROC, TIC900).

Dusek U, Cosijn MM, Ni H, et al. (2019) Technical note: An automated system for separate combustion of elemental and organic carbon for 14C analysis of carbonaceous aerosol. *Aerosol and Air Quality Research* 19(11): 2604-2611.

Dusek U, Monaco M, Prokopiou M, et al. (2014) Evaluation of a two-step thermal method for separating organic and elemental carbon for radiocarbon analysis. *Atmospheric Measurement Techniques* 7(7): 1943-1955.

Edgar RC, Haas BJ, Clemente JC, et al. (2011) UCHIME improves sensitivity and speed of chimera detection. *Bioinformatics* 27(16): 2194-2200.

Fu X, Zhang H, Liu C, et al. (2019) Significant seasonal variations in isotopic composition of atmospheric total gaseous mercury at forest sites in China caused by vegetation and mercury sources. *Environmental Science & Technology* 53(23): 13748-13756.

Fu XW, Heimburger LE and Sonke JE (2014) Collection of atmospheric gaseous mercury for stable isotope analysis using iodine- and chlorine-impregnated activated carbon traps. *Journal of Analytical Atomic Spectrometry* 29(5): 841-852.

Han Y, An Z, Arimoto R, et al. (2022) Sediment soot radiocarbon indicates that recent pollution controls slowed fossil fuel emissions in southeastern China. *Environmental Science & Technology* 56: 1534-1543.

Han YM, Cao JJ, Chow JC, et al. (2007a) Evaluation of the thermal/optical reflectance method for discrimination between char- and soot-EC. *Chemosphere* 69: 569-574.

Han YM, Cao JJ, Posmentier ES, et al. (2009) The effect of acidification on the determination of elemental carbon, char-, and soot-elemental carbon in soils and sediments. *Chemosphere* 75(1): 92-99.

Han YM, Cao JJ, Yan BZ, et al. (2011) Comparison of elemental carbon in lake sediments measured by TOR, TOT and CTO methods and 150-year pollution history in Eastern China. *Environ Sci Technol* 45(12): 5287-5293.

Han YM, Wei C, Bandowe BAM, et al. (2015) Elemental carbon and polycyclic aromatic compounds in a 150-Year sediment core from Lake Qinghai, Tibetan Plateau, China: Influence of regional and local sources and transport pathways. *Environmental Science & Technology* 49(7): 4176-4183.

Han YN, Cao JJ, An ZS, et al. (2007b) Evaluation of the thermal/optical reflectance method for quantification of elemental carbon in sediments. *Chemosphere* 69: 526-533.

Hou X, Zhou W, Chen N, et al. (2010) Determination of ultralow level I-129/I-127 in natural samples by separation of microgram carrier free iodine and accelerator mass spectrometry detection. *Analytical chemistry* 82: 7713-7721.

Liu W, Wang Z, Wang Z, et al. (2011) Variations in nitrogen isotopic values among various particle-sized fractions in modern soil in northwestern China. *Chinese Journal of Geochemistry* 30(3): 295.

Qiao J, Hou X, Roos P, et al. (2009) Rapid determination of plutonium isotopes in environmental samples using sequential injection extraction chromatography and detection by inductively coupled plasma mass spectrometry. *Analytical chemistry* 81: 8185-8192.

Richter H and Howard JB (2000) Formation of polycyclic aromatic hydrocarbons and their growth to soot--a review of chemical reaction pathways. *Progress in Energy and Combustion Science* 26(4-6): 565-608.

Rose NL (1994) A note on further refinements to a procedure for the extraction of carbonaceous fly-ash particles from sediments. *Journal of Paleolimnology* 11(2): 201-204.

Rose NL (2008) Quality control in the analysis of lake sediments for spheroidal carbonaceous particles. *Limnology and Oceanography-Methods* 6: 172-179.

Ruff M, Wacker L, Gaeggeler HW, et al. (2007) A gas ion source for radiocarbon measurements at 200 kV. *Radiocarbon* 49(2): 307-314.

Sherwood AR and Presting GG (2007) Universal primers amplify a 23S rDNA plastid marker in eukaryotic algae and cyanobacteria. *Journal of phycology* 43(3): 605-608.

Synal H-A, Stocker M and Suter M (2007) MICADAS: A new compact radiocarbon AMS system. *Nuclear Instruments & Methods in Physics Research Section B-Beam Interactions with Materials and Atoms* 259(1): 7-13.

Tjallingii R, Röhl U, Koelling M, et al. (2007) Influence of the water content on X-ray fluorescence core-scanning measurements in soft marine sediments. *Geochemistry Geophysics Geosystems* 8.

Wacker L, Bonani G, Friedrich M, et al. (2010) MICADAS: Routine and high-precision radiocarbon dating. *Radiocarbon* 52: 252-262.

Wang Y, Sheng HF, He Y, et al. (2012) Comparison of the levels of bacterial diversity in freshwater, intertidal wetland, and marine sediments by using millions of illumina tags. *Applied and Environmental Microbiology* 78(23): 8264-8271.

Wei C, Bandowe BAM, Han Y, et al. (2015) Polycyclic aromatic hydrocarbons (PAHs) and their derivatives (alkyl-PAHs, oxygenated-PAHs, nitrated-PAHs and azaarenes) in urban road dusts from Xi'an, Central China. *Chemosphere* 180: 128-137.

Xing S, Zhang W, Qiao J, et al. (2018) Determination of ultra-low level plutonium isotopes (Pu-239,240) in environmental samples with high uranium. *Talanta* 187: 357-364.

Yan D, Xu H, Lan J, et al. (2020) Warming favors subtropical lake cyanobacterial biomass increasing. *Science of the Total Environment* 726: 138606.

Yan D, Xu H, Yang M, et al. (2019) Responses of cyanobacteria to climate and human activities at Lake Chenghai over the past 100 years. *Ecological Indicators* 104: 755-763.

Zhang L, Hou X, Li H-C, et al. (2018) A 60-year record of I-129 in Taal Lake sediments (Philippines): Influence of human nuclear activities at low latitude regions. *Chemosphere* 193: 1149-1156.

Zhang L, Zhou W, Hou X, et al. (2011) Level and source of 129I of environmental samples in Xi'an region, China. *Science of The Total Environment* 409(19): 3780-3788.